POLITECNICO DI TORINO

Master's Degree Thesis in Mechanical Engineering

Model Predictive Control for Active Suspension of Electrodynamic Levitation System with Augmented Kalman Filter

Supervisors

Prof. Nicola AMATI

Prof. Renato GALLUZZI

Dr. Eugenio TRAMACERE

Dr. Marius PAKSTYS

Candidate

Keyvan DELFARAH

April 2024

Abstract

Suspension control stands as a fundamental technique in magnetic levitation (Maglev) trains where ensuring the comfort of passengers is paramount. The increasing demand for fast, safe, and efficient transportation systems in recent years has made the design of high-velocity trains, such as Maglevs, inevitable. This project, first addresses the issue of magnetic pad oscillations. Further, a state-of-the-art Model Predictive Controller (MPC) is introduced , which relies on prior knowledge of the system's states for prediction. Additionally, an augmented Kalman filter (AKF) is employed to estimate the desired states for control. The performance of the latter is then compared to experimental results obtained from a test bench. Ultimately, it is demonstrated that MPC outperforms passive damping and active suspension with a static gain controller (LQR).

Acknowledgements

I would like to express my heartfelt gratitude to my parents for their unwavering support throughout my academic journey and for their encouragement to pursue studies abroad. Their endless belief in my abilities has been a constant source of strength and motivation. I am also deeply thankful to my grandparents, whose encouragement from a young age instilled in me a passion for learning and striving for excellence.

I extend my sincere appreciation to Marius, my co-supervisor, whose guidance and support were invaluable throughout this thesis. His mentorship transcended the role of a supervisor, and without his insightful advice, this work would not have been possible. I would also like to extend my gratitude to Prof. Galluzi and Dr. Tramarcere for their valuable contributions and support throughout the thesis.

Special thanks to Prof. Amati, my Supervisor, for granting me the opportunity to be part of this project and for his continuous guidance and encouragement.

I am grateful to my dear friend, Amirhossein, for his unwavering support and motivation during challenging times.

I am deeply indebted to all those mentioned above for their invaluable contributions and unwavering support, which have played a significant role in the completion of this thesis.

Table of Contents

Abstract III

Acknowledgements V

List of Tables IX

List of Figures X

1 Introduction 1

2 Model identification 5
2.1 Mathematical Model 5
2.1.1 System Configuration Space 5
2.1.2 Voice Coil Actuator 8
2.1.3 State Space Transformation 9
2.2 Testbench 11
2.2.1 Dynamic Measuring Device 12
2.2.2 Track Profile 13
2.2.3 2D vertical configuration identification 14

3 Control Strategy 17
3.1 Model Predictive Control 17
3.1.1 Methodology 19
3.1.2 MPC Setup 24
3.1.3 Initial Parameter Selection 26
3.1.4 Sensitivity Analysis 28
3.1.5 Optimal Parameter Selection 28
3.1.6 MPC Optimal Performance Results with Fullstate Feedback 30
3.1.7 MPC Performance Comparison with LQR Controller 36

4 State Observer 39
4.1 Kalman Filter . . . 40
4.1.1 Mathematical Statement . . . 40
4.1.2 Augmented Kalman Filter . . . 44
4.2 Relative velocity Estimation . . . 46
4.2.1 Estimation Model . . . 46
4.2.2 Data Acquisition Setup . . . 48
4.2.3 Experimental Results Considering a Constant VCA Resistance ($\mathbf{R_{vc}} = \mathbf{cte}$) . . . 51
4.2.4 Estimation Model with Offline Resistance Update, $\mathbf{R_{vc}} = \mathbf{R_{vc}(t)}$ 56

5 Evaluation on MPC Performance using Estimated Relative Velocity by AKFVG 67
5.1 MPC Performance Assessment in Presence of Measured Disturbance 67
5.2 MPC Performance Assessment in Absence of Measured Disturbance 68

6 Final Remarks 73
6.1 Conclusions . . . 73
6.2 Further Work . . . 74

A Matrices 77
A.1 State Space for System with Fully Observable Mechanical States (Absolute Kinematic States) . . . 77
A.2 State Space for System with Fully Observable Electromechanical States (Absolute Kinematic States . . . 78
A.3 State Transformation Matrix . . . 79
A.4 State Space for System with Fully Observable Electromechanical Transformed States . . . 79

Bibliography 81

List of Tables

2.1 Electrodynamic levitation system main components.*Source*:[8] . . . 12
2.2 System physical (mechanical & electrical) properties 15

3.1 Weighting values of parameters for the initial setup 26
3.2 Grid search parameters of sensitivity analysis: Stage 1: Initially provides the proximity of the optimal weighting parameters. Stage 2: Yields the precise location of the optimal solution based on the results from Stage 1 29
3.3 Tuned values of parameters 30

4.1 Kalman filter parameters 49
4.2 Experimental tests parameters 59

List of Figures

1.1 Hyperloop capsule rendering. Source: www.hyperlooptt.com 2

2.1 Quarter-car model of electrodynamically levitated pod 5

2.2 Equivalent circuit of the current path inside the track conductor with multiple branches in electrical parallel 6

2.3 Quarter-car model of electrodynamically levitated pod using equivalent stiffness k_p 7

2.4 Voice coil cross section and circuit. The force F_{vc} is exerted through the voice coil mover. Electric circuit with impedences R_{vc} , L_{vc} , voltage source V and back electromotive force E_{vc}, ... 9

2.5 Voice coil section and circuit. The force F_{vc} is exerted through the voice coil mover. Electric circuit with impedences R_{vc} , L_{vc} , voltage source V and back electromotive force E_{vc}. 10

2.6 State space transformation scheme: Linear, nonsigular transformation matrix, T, mapping the state vector, $x(t)$, to the new state vector, $\bar{x}(t)$. 10

2.7 Proposed test bench. (1) Structure; (2) support block for micrometric stage; (3) shaft; (4) copper track; (5) aluminum disk; (6) servomotor. *Source*:[8] 11

2.8 Halbach configuration of the PM pad used in testbench experimental validation. F_{drag} and F_{lift}, denote the drag and lift forces, respectively, and v, indicates the peripheral speed of the track. *Source*:[8] 12

2.9 Assembly of equipment required for dynamic experiments. (1) Micrometric stage; (2) unsprung mass; (3) sprung mass; (4) stator-sprung mass flex hinge; (5) voice coil mover fixed to the unsprung mass; (6) voice coil stator fixed to the sprung mass; (7) unsprung–sprung mass flex hinge; (8) sprung mass accelerometer; (9) unsprung mass accelerometer. *Source*:[8] 13

2.10 Copper track profile of the testbench using the first 5 harmonics of the spatial frequencies obtained through measurements. (a) Approximate height of the track centreline (b) Magnified deviation of track profile ($\times 5 \cdot 10^3$) (testbench is not accurately scaled) 14

3.1 Geometrical representation of quadratic cost function: (a) A generic quadratic cost function with one global minimum, (b) Convex and non-convex set 18
3.2 Function principle of a model-based predictive with horizons N1, N_u, N_p 18
3.3 MPC algorithm scheme: The figure represents the general scheme of an MPC algorithm. The prediction and optimization takes place within the MPC block and the optimal input is fed into the controlled plant. The measured output is used to update the prediction at each iteration. 20
3.4 Simulink base model used for the MPC setup 24
3.5 Comparison of MPC and passive damping for vibration control of sprung mass: (a) sprung mass displacement comparison, z_s (b) sprung mass acceleration comparison, $\ddot{z_s}$ 27
3.6 Sensitivity analysis of the tunable parameters $w_{\Delta u}$ and $w_{i_{vc}}$ in stage 1:(a) Exhibits the performance index of tuning parameters based on offset RMS values of z_s (b) Exhibits the contour map of the pertaining 3D surface 31
3.7 Sensitivity analysis of the tunable parameters $w_{\Delta u}$ and $w_{i_{vc}}$ in stage 2:(a) Exhibits the performance index of tuning parameters based on offset RMS values of z_s (b) Exhibits the contour map of the pertaining 3D surface 32
3.8 Comparison of MPC and passive damping for vibration control of sprung mass with optimal tuning of MPC: (a) sprung mass displacement comparison, z_s (b) sprung mass acceleration comparison, $\ddot{z_s}$ 33
3.9 Comparison of MPC and passive damping for the displacement of unsprung mass with optimal tuning of MPC 34
3.10 Acting forces on the sprung mass: The figure shows the sum of internal forces arising from the viscous damper and elastic spring (blue line), the actuation force coming from the VCA, $k_m i_{vc}$, (red line), and the residual force remaining in the sprung mass as the difference between the internal and actuation force (orange dashed line). 35
3.11 The Comparison of the effectiveness of the actuation force on the the sprung mass displacement z_s 36

3.12 Performance comparison of MPC, LQR, and passive damping control, based on sprung mass displacement, z_s 37
3.13 Performance comparison of MPC, LQR, and passive damping control, based on sprung mass acceleration, $\ddot{z}_s$ 37
3.14 Comparison of the input force for the case of MPC and LQR controller 38

4.1 Probability density functions associated with the prediction (blue), measurement update (red), and the fusion (green) stages of Kalman filter algorithm for an individual state 43
4.2 Closed loop feedback control of a generic LTI system scheme augmented with state estimator: $\hat{x}$ and x denote the estimated states and real states, and $\hat{z}$ and z represent the estimated outputs and measured outputs. 45
4.3 State observer model for the estimation of relative velocity through estimation of induced voltage, E_{vc} 47
4.4 Hardware setup for the data acquisition from testbench 49
4.5 Detailed view of the LAUNCHXL-F28379D microcontroller 50
4.6 Software setup for the data acquisition from testbench 51
4.7 VCA Current comparison between the simulation and Kalman filter estimation from experimental data: (a) the time interval is considered to be 80 seconds to showcase the general profile of the relative velocity (drift) (b) zoomed view 52
4.8 Relative velocity comparison between the simulation and Kalman filter estimation from experimental data: (a) the time interval is considered to be 80 seconds to showcase the general profile of the relative velocity (drift) (b) zoomed view 53
4.9 Relative velocity comparison between the simulation and Kalman filter estimation from experimental data with retuned VCA resistance ($R_{vc} = 1.485\Omega$): (a) the time interval is considered to be 80 seconds to showcase the general profile of the relative velocity (drift) (b) one second snapshot of (a) for profile comparison 55
4.10 Approximated resistance of the VCA coil using the relation $R = \frac{V}{I}$. 56
4.11 Simulink model for augmented Kalman filter wit resistance update 58
4.12 Relative velocity comparison between the simulation and AKFVG estimation from experimental data for test 1 (a) the time interval is considered to be 80 seconds to showcase the general profile of the relative velocity (drift) (b) one second snapshot of (a) for profile comparison 60

4.13 Relative velocity comparison between the simulation and AKFVG estimation from experimental data for test 2 (a) the time interval is considered to be 80 seconds to showcase the general profile of the relative velocity (drift) (b) one second snapshot of (a) for profile comparison 61
4.14 Relative velocity comparison between the simulation and AKFVG estimation from experimental data for test 3 (a) the time interval is considered to be 80 seconds to showcase the general profile of the relative velocity (drift) (b) one second snapshot of (a) for profile comparison 62
4.15 Relative velocity comparison between the simulation and AKFVG estimation from experimental data for test 4 (a) the time interval is considered to be 80 seconds to showcase the general profile of the relative velocity (drift) (b) one second snapshot of (a) for profile comparison 63
4.16 Relative velocity comparison between the simulation and AKFVG estimation from experimental data for test 5 (a) the time interval is considered to be 80 seconds to showcase the general profile of the relative velocity (drift) (b) one second snapshot of (a) for profile comparison 64

5.1 Sprung mass displacement comparison for the cases with passive damping and MPC with feedback from estimated relative velocity (a) model simulation for 10 seconds (b) zoomed view 69
5.2 Sprung mass acceleration comparison for the cases with passive damping and MPC with feedback from estimated relative velocity (a) model simulation for 10 seconds (b) zoomed view 70
5.3 Sprung mass displacement comparison for the cases with passive damping and MPC with feedback from estimated relative velocity with no measured disturbance (a) model simulation for 10 seconds (b) zoomed view 71

Chapter 1

Introduction

In recent decades, globalization and growing environmental awareness have catalyzed significant shifts in the mobility landscape. Future transport systems aspire to seamlessly connect major urban centers using sustainable, rapid, safe, and efficient technologies. Governments worldwide are actively addressing these priorities through various initiatives. For instance, the Strategic Transport Research and Innovation Agenda (STRIA) of the European Union focuses on advancing transport electrification and smart mobility solutions [1].
In this context, the Hyperloop concept has emerged as a promising future transportation system. Inspired by Robert Goddard's vactrain concept [2], the Hyperloop involves levitating capsules traveling inside an evacuated tube. Thanks to the low-pressure environment and advanced levitation technology, the capsules experience minimal friction with any medium, enabling speeds exceeding 1200 km/h, Figure 1.1. This remarkable speed capability allows for rapid traversal of vast distances in relatively short timeframes, effectively bridging the gap between urban areas. Additionally, the Hyperloop embodies an environmentally-friendly paradigm, as its levitation and propulsion systems operate on fully electrified principles, contributing to zero-emission mobility. The modern Hyperloop system was introduced in a white paper published by SpaceX in 2013 and subsequently made available as an open-source design [3]. This conceptual framework envisioned capsules levitated through air bearings and propelled by a linear induction motor and axial compressors. The design rationale behind this configuration stems from the impracticality of employing wheels or any form of mechanical contact with the track at extremely high speeds. However, the concept underwent further refinement, transitioning to the utilization of magnetic pads akin to the Inductrack concept, thus enhancing the system's operational efficiency and performance.
By replacing air bearings with magnetic pads in the Indutrack this idea became evolved [4]. This system operates based on the principle of electrodynamic levitation, where a capsule outfitted with permanent magnets generates a magnetic field that

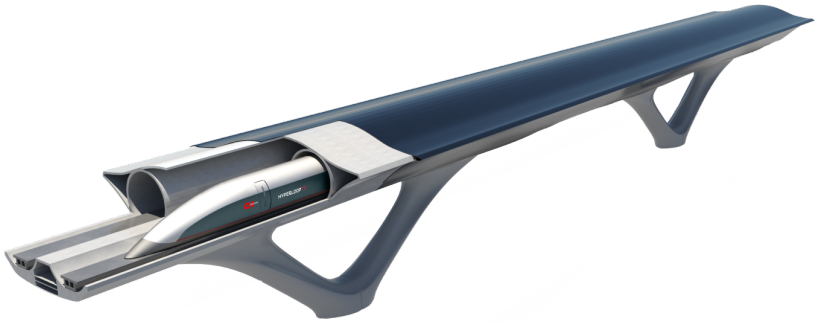

Figure 1.1: Hyperloop capsule rendering. Source: www.hyperlooptt.com

interacts with a conducting track. This interaction induces eddy currents within the track, resulting in lift and drag force components. The levitation architecture facilitated by this mechanism allows for large air gaps, ensuring self-reliability, a low component count, and simplicity in design. Moreover, this approach is entirely passive, eliminating the need for cryogenic cooling systems typically associated with superconducting electrodynamic levitation methods. The lift-to-drag ratio increases with speed, rendering the Inductrack technology highly attractive for very high-speed applications. In this context, the Hyperloop concept emerges as a compelling and more efficient alternative to traditional transportation systems.
The levitation subsystem serves as a crucial enabling technology in the Hyperloop concept. Of particular interest is the implementation of stable, passive levitation achieved through electrodynamic means. In this regard, scientific research conducted in the field of electrodynamic bearings (EDB) for rotating machines serves as a valuable point of reference.

Several studies have been conducted in identification and modelling of different configurations of the EDBs and characterization of their unstable behaviour and approaches to stabilize their dynamic behaviour. This includes the minimum passive damping required for the task of stabilization [5, 6]. To reproduce the force behavior in levitation, General Atomics provided a setup using a rotating conductive drum and a permanent-magnet array. The rig layout described has been replicated and investigated by numerous research groups with similar objectives. In many of these studies, significant challenges arise when attempting to reproduce the force behavior using analytical models, primarily due to heavy nonlinear contributions observed at high speeds.
Addressing the instability issue of levitating systems, a further study have been conducted upon increasing the degree of the freedom of the system, using a secondary mass[7].
For the purpose of suspension several control techniques have been utilized. These

techniques vary from semi-active control strategies such as skyhook and groundhook damping, to optimal controllers such as Linear Quadratic Regulator (LQR) and rule based ones such as fuzzy logic controller.
A well suited control strategy to satisfy the task of robust control is a model based optimal control strategy, referred to as Model Predictive Control (MPC). MPC relies on readily available models, prevalent across disciplines, thereby leveraging existing knowledge without the need for explicitly formulating complex control laws—a task typically reserved for control experts. Instead, MPC automatically derives the control law via model-based optimization. Its implicit formulation, adaptability, and reliance on models stand as the primary advantages of MPC. These facets advocate for the widespread adoption of MPC within the engineering community.
The advantage of using MPC in a control system with respect to similar strategies such as LQR is the its capability in handling external constraints on the system inputs and outputs. This feature is a key parameter in using such control strategy where in real world applications often there are physical limitations.
Using the 2 DoF model presented in [7], the present research studies the ability of a linear MPC in isolating the electrodynamic excitations induced from the track and transfer into the secondary mass that is referred to as unsprung mass in automotive fields. However, adopting such advanced strategy requires careful tuning of the pivotal parameters that overcome the final output of the system. For this reason a sensitivity analysis on the aforementioned parameters are conducted to result in the ideal compromise.
In addition to the control a further study is being done on observing the unmeasurable states of the system. This issue is particularly addressed when a model based controller such as MPC is employed. This project provides a novel approach using the augmented Kalman filter for the estimation purpose for case in which the physical properties of the system change with respect to time. For the validation purpose, the proposed approach is being tested in the testbench and the experimental results are being compared to that of numerical simulations. Eventually, the validated estimation model is being employed in the closed loop model using MPC.

Chapter 2

Model identification

2.1 Mathematical Model

2.1.1 System Configuration Space

The mathematical model that is describing the system dynamics is a quarter-car configuration due to its prevalent similarities with conventional automotive systems. According to [7], a system of one degree of freedom (DoF) exhibits instability and is the main rational that leads to design of a system of two Dof. In this case, the system is comprised of two lumped masses, two elastic springs, an actuator (voice coil), a viscous damper, and the track profile, Figure 2.1.

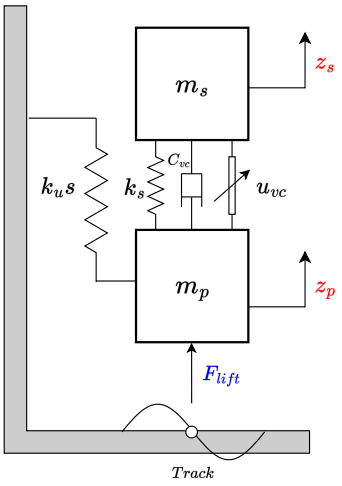

Figure 2.1: Quarter-car model of electrodynamically levitated pod

To showcase the levitation model, an equivalent circuit of the current path within the track conductor is utilized, featuring multiple branches in electrical parallel,

Figure 2.2. Each branch contains a resistor and an inductor in series, and the

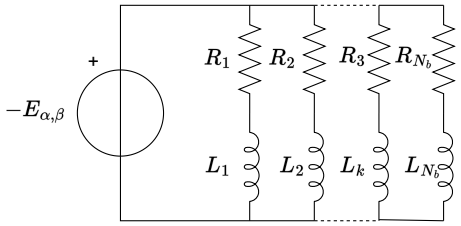

Figure 2.2: Equivalent circuit of the current path inside the track conductor with multiple branches in electrical parallel

overall branches are parallel together with a voltage generator representing a Back Electromotive Force (back-emf). Using Kirchhoff's Voltage Law (KVL) for each branch, the balance of terms for the k-th branch is indicated in Equation (2.1).

$$L_k \frac{di_k}{dt} + R_k i_k + E_{vc} = 0 \tag{2.1}$$

To transform from static to rotating frame through $i_k = i_{r,k} e^{jwt}$, the expression of the current and BEMF through become in terms of direct and quadrature axis components, since $i_{r,k} = i_{d,k} + j i_{q,k}$. Furthermore, the impedance of the k-th branch can be described by means of the introduction of the electromagnetic pole frequency, $\omega_{p,k} = \frac{R_k}{L_k}$ that yields the expression of the current change rates through Equation (2.2).

$$\begin{aligned} \frac{di_{d,k}}{dt} &= -\omega_{p,k} i_{d,k} + \omega i_{q,k} - \frac{E_d}{L_k} \\ \frac{di_{q,k}}{dt} &= -\omega_{p,k} i_{q,k} + \omega i_{d,k} - \frac{E_q}{L_k} \end{aligned} \tag{2.2}$$

According to Equation (2.2), there is an evident dependency of the direct component on the quadrature component and vice versa. Using Equation (2.2), one can obtain a power balance model of the circuits. The governing power balance equations of the model is comprised of three pair of terms indicating, the rate of change of stored magnetic energy, the dissipated power by the Jule effect, and the last pair belonging to the mechanical power developed by the levitation system, from which lift and drag forces can be computed, Equation (2.3).

$$\begin{aligned} F_{lift} &= \frac{E_d}{\dot{z}_p} \sum_{k=1}^{N_b} i_{d,k} = \frac{\partial \Lambda}{\partial z_p} \sum_{k=1}^{N_b} i_{d,k} \\ F_{drag} &= -\frac{E_d}{v} \sum_{k=1}^{N_b} i_{q,k} = -\frac{\Lambda}{\gamma} \sum_{k=1}^{N_b} i_{q,k} \end{aligned} \tag{2.3}$$

In this context, the investigation excludes considerations related to horizontal components and rotational forces about the pertaining axes, i.e. the sole focus remains on understanding and assessing the system's behavior, specifically concerning its vertical dynamics and stability. Referring to Figure 2.1, F_{lift} denotes the vertical component of the magnetic force developed by the levitation system. It can be shown that the lift force depends on the flux linkage, the vertical displacement, pole-pitch ratio, and the direct current that is coupled with the quadrature component. Due to the nonlinear definition of flux linkage, lift force displays exponential behavior. In this case, it is possible to substitute the force with an elastic component through mathematical manipulation. In literature, the levitation system is usually modeled using an equivalent stiffness representation [7]. This parameter can be calculated as:

$$k_p = \frac{\partial F_{lift}}{\partial z_p} \tag{2.4}$$

The explicit definition of the k_p is independent from the vertical displacement or the longitudinal speed. It can be shown that k_p is depending on the pole-pitch ratio of the magnets and the system total mass through, Equation (2.5).

$$k_p = \frac{2m_t g}{\gamma} \tag{2.5}$$

This expression affords a complete representation of the system's behavior in mechanical domain without losing its generality. Employing an equivalent elastic single term offers mathematical simplicity and reduces computational overhead. Figure 2.3, indicates the case that is the lift force is substituted with the elastic spring, k_p. The model represented in Figure 2.3, resembles that of quarter car

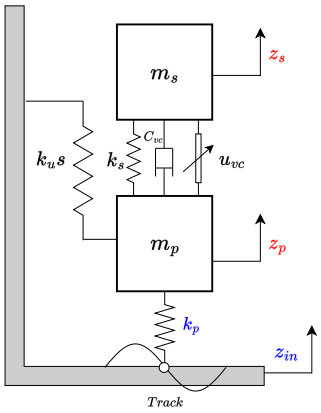

Figure 2.3: Quarter-car model of electrodynamically levitated pod using equivalent stiffness k_p

model in automotive fields. Using a fully mechanical configuration to represent the

system must account for the excitation forces due to the imposed lift force. In a fully mechanical system this term can be modeled as road irregularities likewise to automotive suspension systems. z_{in} denotes the road profile which in our case is the track surface curvature that is obtained from a previous measurement. The absolute displacement of k_p due to the instantaneous difference between z_p and z_{in} provides the pertaining force. In order to derive the equations of motion, Newton's second law is employed. Isolating each of the masses, and keeping the external interactions, namely forces, the set of governing differential equations of motion can be expressed in Equation (2.6).

$$\begin{aligned} &m_s\ddot{z_s} + k_s\left(z_s - z_p\right) + C_{vc}\left(\dot{z_s} - \dot{z_p}\right) + u_{vc}\left(t\right) = 0 \\ &m_p\ddot{z_p} + k_{us}z_p + k_s\left(z_p - z_s\right) + k_p\left(z_p - z_{in}\right) + C_{vc}\left(\dot{z_p} - \dot{z_s}\right) - u_{vc}\left(t\right) = 0 \end{aligned} \tag{2.6}$$

z_i, $\dot{z}_i$,$\ddot{z}_i$, denote absolute displacement, absolute velocity, and absolute acceleration of each mass with respect to an inertial reference frame, respectively. m_i denotes the inertial masses, C_{vc}, is the damping coefficient of the voice coil due to Eddy current1, k_s, is the stiffness of the elastic element in between the masses, k_{us}, is the stiffness of the unsprung mass spring, and z_{in}, the measured track irregularities, where, subscripts s and p refer to the sprung and unsprung masses, respectively. The model represented in the Equation (2.6), points out the system's behavior in dynamic configurations, i.e. it disregards the contribution of the gravitational forces due to the masses' weights. It is due to the fact that that fraction of the control force that is responsible for the attenuation of the dynamic disturbances is independent from the static force provided to decouple the masses (offset force). The term u_{vc}, in the model is the control input that is to provide the demanding offset force to decouple the two masses (static configuration), and to provide the optimal control force to attenuate the impact of disturbances (dynamic configuration). In a fully mechanical model, as mentioned the control input is a force. However, to provide such force, an electromechanical device is needed that is referred to as *voice coil*.

2.1.2 Voice Coil Actuator

A voice coil actuator (VCA), operates based on the principle of electromagnetic induction. It consists of a coil of wire (the voice coil) that, when subjected to an electrical current, generates a magnetic field. This magnetic field interacts with a permanent magnet's field, resulting in a force that drives linear motion. These actuators are prized for their precision, rapid response times, and controlled motion. Figure 2.4, depicts the scheme of the voice coil. As per definition, a voice coil can use the input signal, amplify it by means of external power supply and provide a force that is proportional to the voice coil current. The electrical domain of a voice coil actuator can be modeled with a simple series circuit characterized by

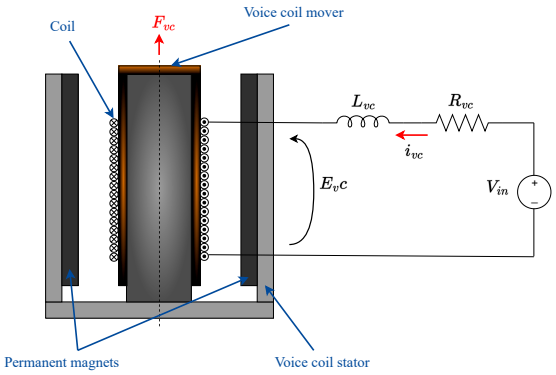

Figure 2.4: Voice coil cross section and circuit. The force F_{vc} is exerted through the voice coil mover. Electric circuit with impedences R_{vc} , L_{vc} , voltage source V and back electromotive force E_{vc},

impedance terms R_{vc} and L_{vc}, an input voltage source V_{in} and a back electromotive force E_{vc}, [8]. Kirchhoff's voltage law is applied for the electric circuit of the VCA leading to the following equation,

$$\begin{aligned} L_{vc}\frac{d_{i_{vc}}}{d_t} + R_{vc}i_{vc} + E_{vc} &= V_{in} \\ E_{vc} &= k_v(\dot{z_s} - \dot{z_p}) \end{aligned} \tag{2.7}$$

Where, k_v, is the back electromotive force constant. This equation fully captures the electrical domain dynamics. However, to account for the electrical domain a further term is needed to interconnect the two domains. The characteristic equation linking the actuation force to the current of the VCA is:

$$u_{vc} = k_m i_{vc} \tag{2.8}$$

Where, k_m, is the force constant with a unit of $[\frac{N}{A}]$. Figure 2.5, illustrates the multidomain model of the levitation system.

2.1.3 State Space Transformation

In the experimental section, the significance of relative velocity between the two masses will be emphasized, as reliance on the absolute velocity of the masses necessitates the use of two sensors to yield the velocities. Furthermore, the primary goal of this project is to estimate the back electromotive force (EMF) in the voice coil actuator, which is linked with the relative velocity between the two masses. To tackle this issue, it is essential to move from absolute states, namely, $\{\dot{z_p}, z_p, \dot{z_s}, z_s\}$ to $\{\dot{z_r}, z_r, \dot{z_s}, z_s\}$, in the kinematic domain, where only the kinematic states of

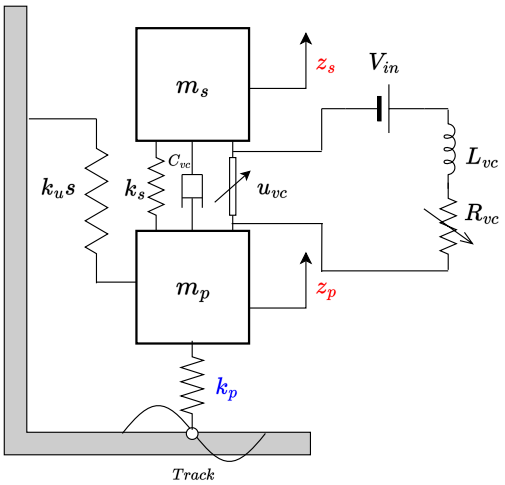

Figure 2.5: Voice coil section and circuit. The force F_{vc} is exerted through the voice coil mover. Electric circuit with impedences R_{vc} , L_{vc} , voltage source V and back electromotive force E_{vc}.

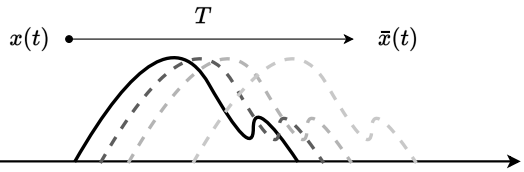

Figure 2.6: State space transformation scheme: Linear, nonsigular transformation matrix, T, mapping the state vector, $x(t)$, to the new state vector, $\bar{x}(t)$.

sprung mass remain absolute. This is accomplished through the utilization of a *Transformation Matrix*, Figure 2.6.
Considering the linear time-invariant (LTI), state space model in canonical form as in Equation (2.9),

$$\begin{aligned} \dot{x}(t) &= Ax(t) + Bu(t) \\ y(t) &= Cx(t) + Du(t) \end{aligned} \tag{2.9}$$

a state space transformation can be obtained using a biunivocal linear transformation which links the old state vector x with the new vector $\bar{x}$:

$$x = T\bar{x} \tag{2.10}$$

where T is a square nonsingular matrix.
Based on the transformed states, the transformed state space matrix becomes:

$$\begin{aligned} \dot{\bar{x}}(t) &= \bar{A}\bar{x}(t) + \bar{B}u(t) \\ y(t) &= \bar{C}\bar{x}(t) + Du(t) \end{aligned} \tag{2.11}$$

Accordingly, the state and input matrices can be described as follow:

$$\bar{A} = T^{-}1AT, \quad \bar{B} = T^{-}1B, \quad \bar{C} = CT \tag{2.12}$$

where $\bar{A}$, $\bar{B}$, $\bar{C}$, represent, state matrix, input matrix, and output matrix, respectively.

2.2 Testbench

Performing a proper test to study the system's behavior requires a long track profile. To tackle this issue a circular track is devised that enables the study for long runs as illustrated in Figure 2.7. The experimental setup features an axial configuration comprising an aluminum disk with a diameter denoted as D_d. Affixed to the disk is a copper ring with an average diameter D_t, a width w_t, and a thickness h_t. The copper ring is fastened to the disk through screws. The entire assembly is coupled to a brushless servomotor, specifically the Kollmorgen® AKM model, which is positioned beneath the primary structure. The speed of the servomotor is regulated by a power converter, the Kollmorgen® AKD, ensuring precise control. The rotating components are housed within a protective chamber, bordered by

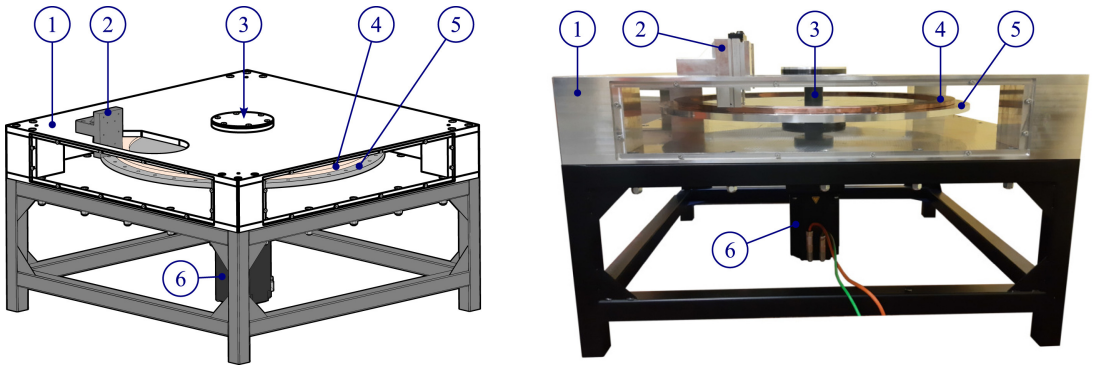

Figure 2.7: Proposed test bench. (1) Structure; (2) support block for micro-metric stage; (3) shaft; (4) copper track; (5) aluminum disk; (6) servomotor. *Source*:[8]

transparent panels to allow visual monitoring. The copper ring functions as a conductive track, allowing for electrodynamic levitation. To induce levitation, a Halbach array pad is used. A Halbach array is a particular configuration of permanent magnets that allows the magnetic field to be strengthened along one face of the array itself. The adopted configuration in the test rig is composed of eight N45UH NdFeB permanent magnets with 45-degree turn, fixed to the bench frame. The arrangement of these magnets follows the magnetization pattern depicted in Figure 2.8. Pad and track features are enlisted in Table 1.

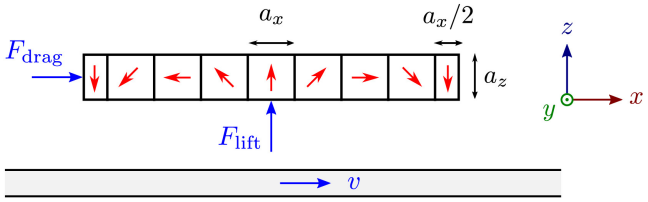

Figure 2.8: Halbach configuration of the PM pad used in testbench experimental validation. F_{drag} and F_{lift}, denote the drag and lift forces, respectively, and v, indicates the peripheral speed of the track. *Source*:[8]

Component	Parameter	Symbol	Value	Unit
N45UH NdFeB PM array	Number of PMs	N_m	8	-
	Length	a_x	12.7	mm
	Width	a_y	63.5	mm
	Height	a_z	12.7	mm
	Remanence	B_t	1.35	T
	Relative magnetic permeability	μ_t	1.05	-
Copper track	Thickness	h_t	15	mm
	Average diameter	D_t	940	mm
	Width	w_t	60	mm
	Resistivity	ρ_t	1.72×10^{-8}	$\Omega \cdot m$

Table 2.1: Electrodynamic levitation system main components.*Source*:[8]

2.2.1 Dynamic Measuring Device

The dynamic set up is a mechanical device comprised of a sprung mass, an unsprung mass and a voice coil, decoupling the masses. The stator configuration comprises two perforated aluminum disks connected through a network of vertical beams. Each element within this structure features specially designed slotted housings, facilitating the secure mounting of spring elements. The stator, firmly affixed to the welded frame using a sledge holder, remains stationary. Conversely, the mechanical linkage with the unsprung mass is established through eight parallel cantilever springs. The connection points between these two components are arranged to restrict any substantial movements, except in the vertical direction. This design choice is evident in the deployment of springs organized into two parallel groups, each consisting of four elements distributed circumferentially. This arrangement inhibits both transversal and rotational motions of the dynamic measuring device, ensuring stability and precise vertical movement.
The unsprung mass serves as a representative model for the hyperloop's bogie. Positioned with the permanent magnets oriented towards the track, the unsprung

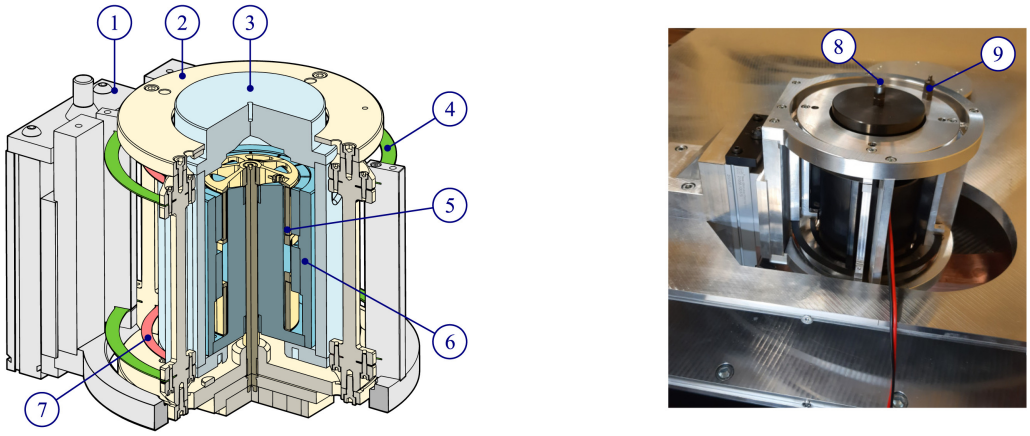

Figure 2.9: Assembly of equipment required for dynamic experiments. (1) Micro-metric stage; (2) unsprung mass; (3) sprung mass; (4) stator-sprung mass flex hinge; (5) voice coil mover fixed to the unsprung mass; (6) voice coil stator fixed to the sprung mass; (7) unsprung–sprung mass flex hinge; (8) sprung mass accelerometer; (9) unsprung mass accelerometer. *Source*:[8]

mass experiences direct exposure to the lift electrodynamic force. Structurally, it replicates the design of the stator, featuring two aluminum plates connected by four vertical beams. By considering the lower disk of the device, the Halbach array can be seen underneath the disk, facing the copper track. Simultaneously, the mover of the voice coil is situated on the opposite side. It is essential to highlight that the unsprung mass is linked to the stator via a series of springs. While this structural damping is deemed insignificant compared to the electromagnetic damping introduced by the voice coil, it is crucial to recognize its negligible impact. However, in scenarios where the voice coil remains inactive, and the system behaves as a single block mass, the damping effect of the springs becomes significant. This structural damping can potentially influence electromagnetic suspension phenomena and act as a preventative measure against instability. Therefore, careful consideration of these dynamic interactions is essential for the overall stability and performance of the electromagnetic suspension system. The sprung mass is designed to emulate the hyperloop pod and includes a ferromagnetic core that houses the voice coil stator. Enhancing the closure of magnetic field lines, this substantial block is capped with a ferromagnetic cover on the top.

2.2.2 Track Profile

Due to the imperfections stemming from the manufacturing process, there are deficiencies with respect to the designed CAD model. The copper track profile displays surface irregularities due to the mechanical tolerance of the surface finishing, [8]. The deviations have been measured by a laser probe fixed on the support

of the test bench. To streamline the representation, the first 5 harmonics of the road profile have been considered for the simulation purpose. The isolation of the frequency is extracted from Fourier transform of the obtained track profile, i.e. the harmonic contribution of the track as a function of the disk angular frequency. This approach allows for an accurate model of the essential characteristics of the actual track irregularities, contributing to a more efficient and manageable representation in the conducted analysis.

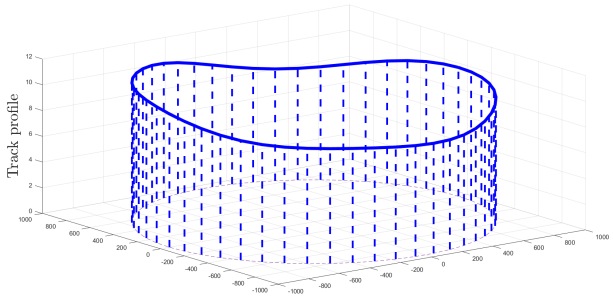

(a)

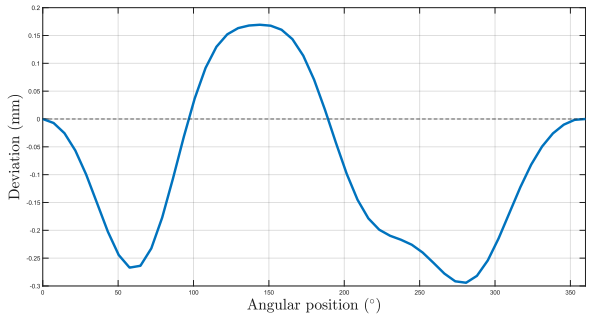

(b)

Figure 2.10: Copper track profile of the testbench using the first 5 harmonics of the spatial frequencies obtained through measurements. (a) Approximate height of the track centreline (b) Magnified deviation of track profile ($\times\ 5 \cdot 10^3$) (testbench is not accurately scaled)

2.2.3 2D vertical configuration identification

The mathematical model illustrated in Figure 2.3, is a simplified model of the test bench representing a 2 DoF mechanical system in a vertical configuration. Considering the analogy between the real system and kinematic scheme of the system, quantities such as system inertial masses obtained through measuring

devices. However, for the identification of the elastic components have been conducted through FEM analysis alongside impact tests, by [9]. The frequency domain analysis through frequency response function (FRF), yields the natural frequencies of the component. Using the first natural frequency the stiffness of each elastic component is obtained having the pertaining mass.
Estimation of the resistance is conducted through evaluating the mean value of the applied voltage and that of the measured current. The inductance estimation of the voice coil involves addressing uncertainties related to temperature, offset frequency, and the contribution of permanent magnets and conductive parts. Experimental estimation is conducted by exciting the voice coil with reversed power cables to simplify the system. Step and sinusoidal signals are employed for assessing static behavior and frequency dependency. Transient and dynamic responses are computed, and static inductance is estimated through a fitting procedure. Dynamic inductance is evaluated considering the mover inside its magnetic housing with sinusoidal signals at various frequencies. The resulting dynamic inductance shows a non-trivial dependency on the offset. The estimated values serve as qualitative reference points, with emphasis on the mean dynamic inductance ($\bar{L}_{vc}$) as a representative measure, considering contributions from magnets and aluminum parts. Referring to Figure 2.3, mechanical properties of the system are enlisted in Table 2.2.

Parameter	**Symbol**	**Value**	**Unit**
Sprung mass	m_s	15.82	kg
Unsprung mass	m_p	4.2	kg
Frame attachment stiffness	k_{us}	9700	N/m
Secondary suspension stiffness	k_s	4422	N/m
Levitation system equivalent stiffness	k_p	2429	N/m
Voice coil damping	C_{vc}	207	N/(m·s)

Table 2.2: System physical (mechanical & electrical) properties

Chapter 3

Control Strategy

3.1 Model Predictive Control

MPC is a set of advanced control strategies that uses the explicit model of the system to predict the future behaviour of the system, within a finite horizon. In the context of model predictive control, this horizon is denoted as the *prediction horizon*, i.e. the interval between the current instant and a predefined future instant of the system that the prediction windows has been set. The prediction horizon holds significant importance; it should be tailored to be sufficiently long to represent the effect of a change in the manipulated variable u on the control variable y while avoiding excessive computational demands [10].
Taking into consideration this prediction, it obtains the sequence of optimal input $u(t)$ by solving a constrained optimization problem. Within the prediction horizon, the optimized input sequence is applied to the prediction model within a predefined period, referred to as the *control horizon*. At $(k+1)$-th instant, only the first element of the optimal input sequence computed at k-th instant, is applied to the system, Figure 3.2.
The cost function that sets the optimization problem, is formulated to minimize the reference tracking error between the given reference and the system output, $e = y - r$. It typically consists of two components: a control performance term, which penalizes deviations from the desired setpoint or trajectory, and a control effort term which penalizes excessive changes in the control inputs. Mathematically speaking, it is often formulated in a quadratic form, rendering a convex problem optimization, Figure 3.1. This convexity property is crucial as it guarantees the existence of a unique global minimum, enabling efficient and reliable optimization algorithms to be employed [11]. In this instance, the cost function of MPC bears

resemblance to that of the *Linear Quadratic Regulator (LQR)* controller. However, the distinguishing feature of MPC lies in its ability to handle constraints, a capability lacking in methods like LQR. This feature is particularly crucial in industrial applications where preventing actuator saturation is paramount. By considering constraints, MPC ensures that control inputs remain within safe operating limits, enhancing system stability and performance in real-world scenarios [12].

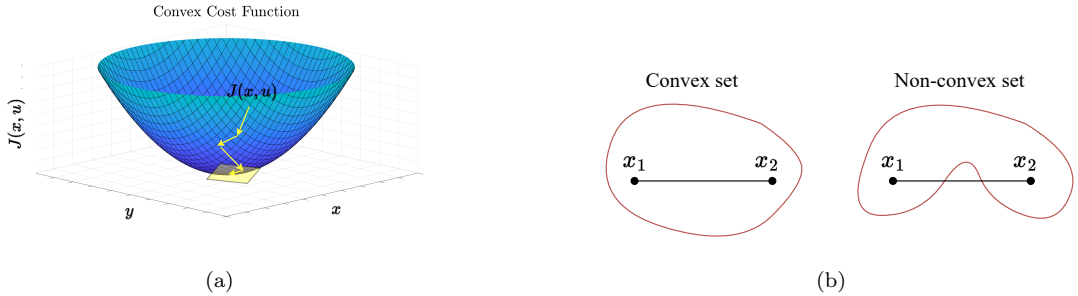

(a) (b)

Figure 3.1: Geometrical representation of quadratic cost function: (a) A generic quadratic cost function with one global minimum, (b) Convex and non-convex set

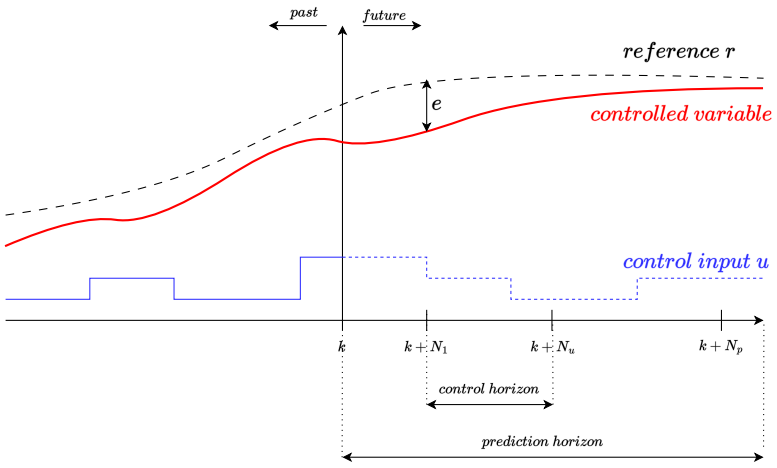

Figure 3.2: Function principle of a model-based predictive with horizons N1, N_u, N_p

One notable drawback of the MPC strategy is its requirement for full state feedback. This arises from the predictive nature of the strategy that relies on observing all states to accurately forecast system behavior. To mitigate this constraint, an additional state observer must be deployed to estimate the unmeasured states. Further elaboration on observation methods will be provided in Chapter 4. This section aims to present the theory behind MPC and its implementation in the simulation of the model.

3.1.1 Methodology

As mentioned, MPC relies on the prediction of the system states to provide the optimal sequences of inputs. Considering a system with linear time invariant (LTI) model in discrete time domain which is compatible with our case, can be considered as follows:

$$\begin{aligned} x(k) &= Ax(k-1) + Bu(k-1) + G\omega(k-1) \\ y(k) &= Cx(k) \end{aligned} \tag{3.1}$$

where $\omega(k-1)$, denotes the disturbance model, i.e. the track irregularities, at instant $t = k-1$. In Equation (3.1), the input vector is decomposed into manipulated variables (control inputs) and disturbance. This is due to the fact that the optimization process is applied only on the controllable inputs (VCA voltage). Using the model, at each consecutive sampling instant $k, k = 1,2,3, ...$, the vector of the future increments of the manipulated variables is obtained online.

$$\Delta \boldsymbol{u}(k) = \begin{bmatrix} \Delta u(k|k) \\ \vdots \\ \Delta u(k+N_u-1|k) \end{bmatrix} \tag{3.2}$$

The expression $\Delta u(k+p|k)$, denotes the increment of the control input in the sampling instant $k+p$, calculated at the current sampling time k. N_u denotes the control horizon defining the number of decision variables. According to Equation (3.2), the increment at the first and last instant within the control horizon is as follows:

$$\begin{aligned} \Delta u(k|k) &= u(k|k) - u(k-1) \\ \Delta u(k+p|k) &= u(k+p|k) - u(k+p-1|k) \end{aligned} \tag{3.3}$$

for $p = 1, ..., N_u - 1$, the symbol $u(k+p|k)$ indicates the value of the control input in the sampling instant $k+p$ obtained in the current instant k. $u(k-1)$ denotes value of the control input in the previous sampling instant $k-1$.
The task of obtaining the optimal sequences of the control inputs, to reduce the tracking error is by solving an optimization problem through minimizing an index performance, $J(r, u_{opt})$.

$$J(k) = \sum_{p=1}^{N_p} \|(r(k+p|k) - \hat{y}(k+p|k)\|^2_{M_p} + \sum_{p=0}^{N_u-1} \|\Delta u(k+p|k)\|^2_{\Lambda_p} \tag{3.4}$$

Equation (3.4) represents the quadratic cost function used for the optimization task, defining the norm $\|x\|^2_A = x^T Ax$, being the matrix A square. $J(k)$ can be decoupled into two components.

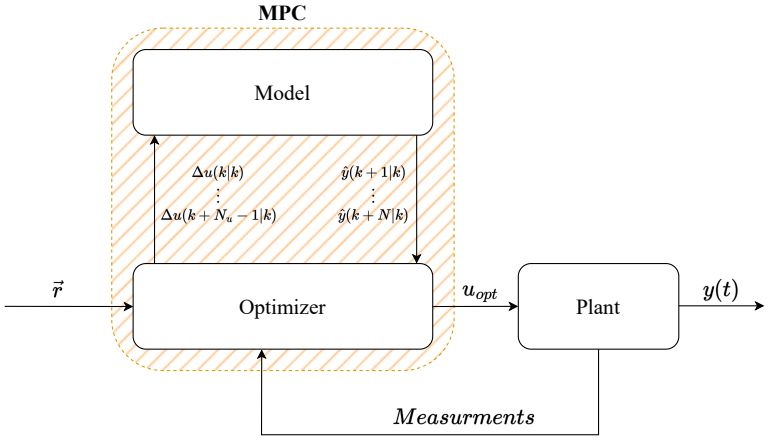

Figure 3.3: MPC algorithm scheme: The figure represents the general scheme of an MPC algorithm. The prediction and optimization takes place within the MPC block and the optimal input is fed into the controlled plant. The measured output is used to update the prediction at each iteration.

The first component aims to minimize the reference tracking error within the control horizon, $T_{\text{sample}} \cdot N_p$. Here, M_p represents a diagonal matrix containing the weighting parameters of the plant's measured outputs, corresponding to the size of the output vector. Each entry of M_p corresponds to an individual output, with a higher value indicating greater importance assigned to the respective output.
The second component penalizes the increment in control input, Δu, over the control horizon N_u. The penalty term, Λp, corresponds to the penalization of the manipulated variables, aimed at minimizing energy consumption. $r(k+p|k)$ is the future value of the reference input that is already known. $\hat{y}(k+p|k)$ indicates the predicted value of the output for the instant $k+p$ at k-th sampling instant, Figure 3.3.
In the case of VCA, limitations on the supplied voltage result in saturation points in the input. These limitations can be modeled as input constraints with upper and lower bounds corresponding to the supply range of the VCA.

$$u_{\min} \leq u(k+p|k) \leq u_{\max}, \quad p = 0, \ldots, N_u - 1 \tag{3.5}$$

In this context, $u_{\min}$ and $u_{\max}$ represent the minimum and maximum values of the manipulated variable, respectively. It is crucial to note that all computed values of the manipulated variable across the entire control horizon are subject to constraints, rather than solely focusing on the value at the current sampling instant $u(k|k)$.
Sudden increment or decrement of the actuator control input as well as the actuator saturation may be problematic. Sudden drop or climax of the force could possibly damage the actuator. To prevent this it is possible to allow the rate of the

manipulated variable be within a certain threshold varying between Δu_{min} and Δu_{max}, as shown in Equation (3.6).

$$\Delta u_{min} \leq \Delta u(k+p|k) \leq \Delta u_{max} \quad p = 0, \ldots, N_u - 1 \tag{3.6}$$

The predicted values of the outputs may as well be limited. In the case of the model under discussion, considering a limited range for the amplitude of the oscillations of the unsprung mass due to design specifications, the displacement of the unsprung mass can't be deliberate. To account for this limitation, it is possible to set constraints for the output values.

$$y_{\min} \leq \hat{y}(k+p|k) \leq y_{\max}, \quad p = 1, \ldots, N \tag{3.7}$$

Referring to the first two sets of constraints, namely, Equations (3.2) and (3.5), the possible solutions of the optimization problem becomes limited. Furthermore, imposing constraints on the predicted outputs, Equation (3.7), may cause some important problems. Often the model is a rough approximation of the actual plant and the process may be affected by a strong disturbance. Being obligated to find an optimal solution, the imposed constraints my bring invisibility issues hindering the process of finding a solution. To tackle this issue, mathematically it is possible to soften the hard constraints on the output variables, Equation (3.7) , when they are not satisfied. Therefore, the predicted values of the outputs may temporarily violate the hard constraints. Softening the constraints on the predicted output variables, the rudimentary MPC optimization problem becomes:

$$\begin{aligned} \min_{\Delta u(k), \epsilon_{\min}(k), \epsilon_{\max}(k)} J(k) = & \sum_{p=1}^{N_p} k \| r(k+p|k) - \hat{y}(k+p|k) \|_2^2 M_p \\ & + \sum_{p=0}^{N_u} \| \Delta u(k+p|k) \|_2^2 \Lambda_p + \rho_{min} \| \epsilon_{\min}(k) \|_2^2 \\ & + \rho_{max} \| \epsilon_{\max}(k) \|_2^2 \end{aligned} \tag{3.8}$$

subject to

$$u_{\min} \leq u(k+p|k) \leq u_{\max}, \qquad p = 0, \ldots, N_u - 1 \tag{3.9}$$

$$\Delta u_{\min} \leq \Delta u(k+p|k) \leq \Delta u_{\max}, \qquad p = 0, \ldots, N_u - 1 \tag{3.10}$$

$$y_{\min} - \epsilon_{\min}(k) \leq \hat{y}(k+p|k) \leq y_{\max} + \epsilon_{\max}(k), \qquad p = 1, \ldots, N \tag{3.11}$$

$$\epsilon_{\min}(k) \geq \mathbf{0}_{n_y \times 1}, \quad \epsilon_{\max}(k) \geq \mathbf{0}_{n_y \times 1} \tag{3.12}$$

When the original hard constraints Equation (3.7), cannot be met, they are temporarily relaxed. This relaxation involves adjusting the minimal and maximal

predicted values of the controlled variables by $\epsilon_{\min}(k)$ and $\epsilon_{\max}(k)$, respectively. In addition to computing the future control increments $\Delta u(k)$, the MPC algorithm also determines vectors $\epsilon_{\min}(k)$ and $\epsilon_{\max}(k)$, each of length n_y, to account for these relaxations.
In Figure 3.3, the schematic representation of a generic plant controlled using MPC is shown. Given the reference input, $\vec{r}$, iteratively based on the sampling time T_s, the controller provides the optimal control action. The control loop is closed with the feedback from measurements. A more comprehensive representation of the MPC algorithm is shown in Algorithm 1.

Algorithm 1 Model Predictive Control (MPC) Algorithm

Initialize:
Set initial state of the system, $k = 0$
Define parameters: T_s, N, N_u, M_p, Λ_p, ρ
Set constraints: $u_{\min}$, $u_{\max}$, $\Delta u_{\min}$, $\Delta u_{\max}$, $y_{\min}$, $y_{\max}$
Set initial guesses for manipulated variables (according to initial condition of the plant): $u(k|k)$, $\Delta u(k|k)$
while not converged **do**
    $k = k + 1$
    Predict:
    Obtain current state of the system
    Predict future states using model: $r(k + p|k)$
    Predict future manipulated variables and the pertaining rates: $u(k + p|k)$, $\Delta u(k + p|k)$
    Predict future prediction error: $\epsilon_{\min}(k)$, $\epsilon_{\max}(k)$
    Cost Function Calculation:
    Calculate the cost function $J(k)$ using the predicted values of $\vec{r}$, ϵ, and manipulated variables
    Optimization:
    Minimize $J(k)$ subject to constraints:
    $u_{\min} \leq u(k + p|k) \leq u_{\max}$, for $p = 0, \ldots, N_u - 1$
    $\Delta u_{\min} \leq \Delta u(k + p|k) \leq \Delta u_{\max}$, for $p = 0, \ldots, N_u - 1$
    $y_{\min} - \epsilon_{\min}(k) \leq \hat{y}(k + p|k) \leq y_{\max} + \epsilon_{\max}(k)$, for $p = 1, \ldots, N$
    $\epsilon_{\min}(k) \geq 0$, $\epsilon_{\max}(k) \geq 0$
    Update Manipulated Variables:
    Select the optimal control inputs that minimize $J(k)$
    Apply Control Action:
    Apply the calculated control inputs to the system
    Update State:
    Measure current state of the system
    Convergence Check:
    Check convergence criteria (e.g., change in cost function, iterations)
end while

3.1.2 MPC Setup

The role of the MPC in this study is to attenuate the oscillations of the sprung mass (capsule). This is analogous to the task of vibration suspension in the automotive field. Essentially, as discussed in Section 2.2.2, the irregularities emerging from the track profile, induce perturbations on the electromagnetic pad. Speaking of passenger comfort in large scale models, this can potentially bring about discomfort. This is the main rational behind adding an active controller namely the MPC further to the passive damping component to actively provide the optimal control input to keep the oscillations of the sprung mass at bellow the discomfort level. It is worth noting that, this task is done by transferring the excitation from the track to the unsprung mass to isolate the sprung mass.
At this stage of the project, it is assumed that all the states of the system are observable and we are able to fully close the feed back loop without any need for an state observer. All the numerical results are simulated in the Matlab Simulink environment. For this purpose, Matlab MPC toolbox is served as the controller agent providing the optimal control input to the plant. The reference input to the MPC block is a vector containing the signals of the equilibrium setpoints for all the outputs.
A state space block is used to mimic the behaviour of the test plant in the continuous time domain. For a system including the transformed electromechanical states, $x_{EM,T} = \{\dot{z}_r, z_r, \dot{z}_s, z_s, i_{vc}\}$, the state space model is described in Appendix A.4.

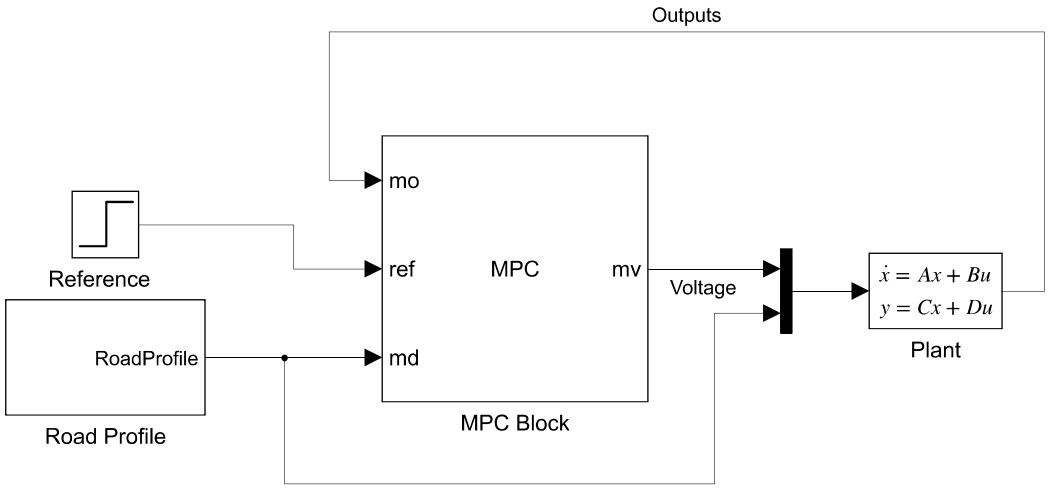

Figure 3.4: Simulink base model used for the MPC setup

As shown in Figure 3.4, the base model that is used for the simulation purpose is comprised of the MPC block, the plant, road profile serving as the disturbance

signal, and the reference input. In a fully observable system without process and measurement noise it is possible to feedback all the Measured Outputs (MO) to the block at each sample. In the model that is used for the test as already mentioned the track profile data exists. This allows for a more precise prediction of the future states of the system, where it is referred to as Measured Disturbance (MD) in the MPC block. Moreover, the case without feeding the track profile signal will be discussed in Section 5.2.
The reference input used in the simulation is a signal vector of size 5×1 with all zero entries. It should be remarked that this is for the case where there is no static forces existing, i.e. the analysis considers the dynamic behaviour of the two masses. In the real case where a lift force is needed to decouple the two masses, this assumption loses its validity due to the constant offset voltage applied to the VCA. For this case the constant value of the VCA current should be fed to the MPC block and the offset displacement of the sprung and unsprung masses should be considered.
Manipulated Variable (MV) port denotes the optimal control input applied to the plant. As can be seen in Figure 3.4, the control input and the disturbance should be discriminated. For this purpose, in the definition of the MPC model, prior to simulation, the input matrix is divided into two columns of MV and MD.
Other parameters that should be set are the sampling time T_s, the prediction horizon N_p, and the control horizon N_u. The choice of sampling time depends on several parameters. Larger sampling time may neglect the essential frequencies that are present in the system. Significantly small sampling time can bring about computational overhead as MPC iteratively should solve an optimization problem at each step. Therefore, the best compromise is to consider the systems dynamics for the selection of an appropriate sampling time. Considering the largest essential frequency of the track profile equal to 287 rad/sec, setting $T_s = 10^3\ Hz$ proved to be an appropriate choice for the simulation. The prediction horizon similar to the sampling time should be long enough to cover the time window that the influence of control input is observable, and short enough not to become computationally time consuming. The choice of control horizon follows the same rational. Accordingly, $N_p = 30$ and $N_u = 2$ are chosen obeying these remarks.
Provided that the VCA can provide up to 250 N of force, the constraints for the voltage input is considered to range between, -10 and 10 volts. Results of the passive damping case show that the amplitude of oscillations for both sprung and unsprung mass is quite negligible with respect to the designed constraints, i.e. the amplitudes are not violating the physical constraints even in the case of passive damping. Therefore, for the output variables no constraints are considered. As a result, the absence of hard constraints on the output variables eliminates the necessity for softening parameters. Moreover, the demanding force for the vibration control of the sprung mass is much smaller than the capability of the VCA to

increment the force at each sampling instant. This further cancels out the need for setting constraints for manipulated variable rates.

3.1.3 Initial Parameter Selection

The choice of appropriate weighting parameters as apposed to the previous parameters needs meticulous analysis of the system. It is possible to mathematically find the optimal set of weighting parameters, however, in practice it is possible to directly search for the relatively optimal parameters through the sensitivity analysis of the system target output with respect to each variable.
Initially, it is supposed that all the parameters hold an even importance in the MPC optimization problem. Accordingly, the weighting parameters of the MPC cost function are defined as 1. It is crucial to point that Simulink uses a term to penalize the absolute value of control input u further to Δu. This is due to the fact that the controller must keep selected manipulated variables at or near specified target values.

Parameter	**Weight**
$\dot{z}_r$	1
z_r	1
$\dot{z}_s$	1
z_s	1
i_{vc}	1
V_{vc}	1
ΔV_{vc}	1

Table 3.1: Weighting values of parameters for the initial setup

Using the values from Section 3.1.3, the performance of the MPC is compared to that of passive damping in Figure 3.5. Observing the results in Figure 3.5, it can be seen that without proper tuning of the MPC parameters not only the system is not capable of attenuating the vibration of sprung mass, its performance is poor with respect to that of passive damping case. In Section 3.1.4, a practical approach based on searching of optimal parameters is elaborated to tackle this issue.

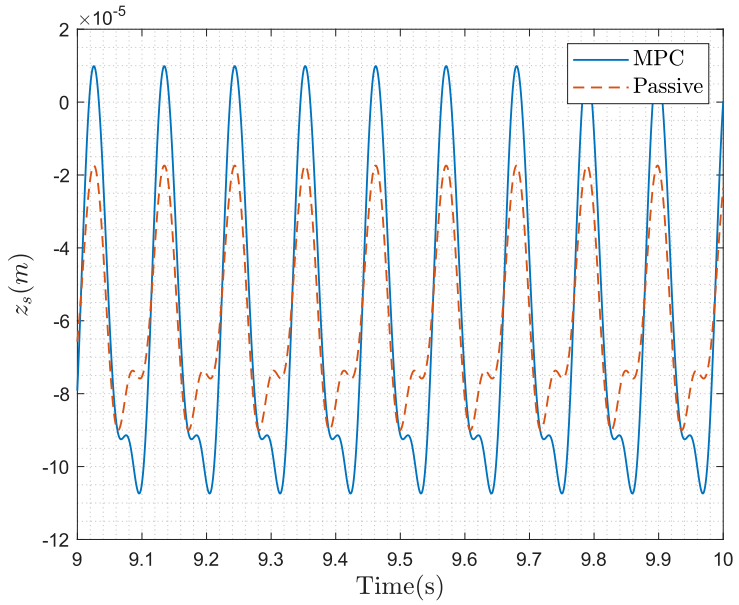

(a)

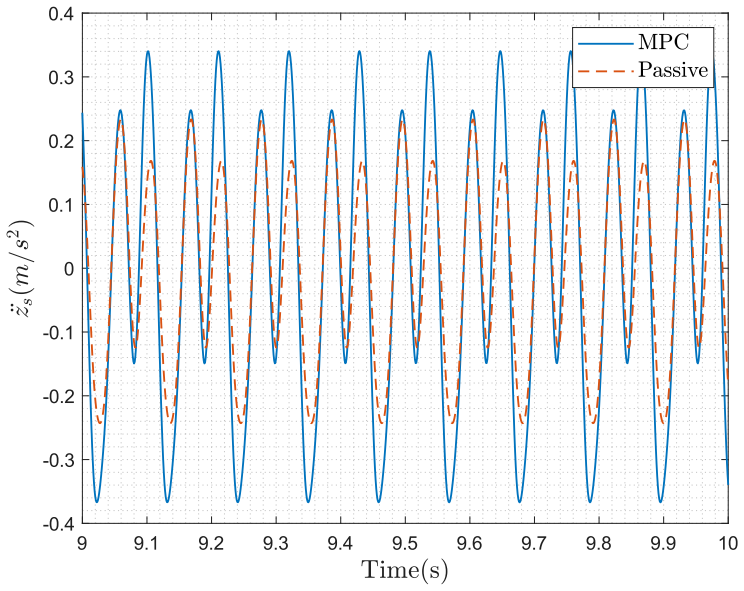

(b)

Figure 3.5: Comparison of MPC and passive damping for vibration control of sprung mass: (a) sprung mass displacement comparison, z_s (b) sprung mass acceleration comparison, $\ddot{z}_s$

3.1.4 Sensitivity Analysis

The performance of Model Predictive Control (MPC) hinges significantly on the design of its cost function. Within the framework of a quadratic cost function incorporating both output and input vectors, the specification of weighting parameters becomes paramount. When considering a diagonal matrix for the output weights, each entry in this matrix dictates the significance attributed to its corresponding target output. Elevating the weight assigned to a particular output amplifies its influence on the overall cost function value. Consequently, the optimization problem seeks a solution to penalize the aforementioned output more than others.
Determining the optimal weighting parameters is often of cumbersome task. As the degree of the freedom for the tunable parameters increase, finding the optimal compromise becomes more challenging, specially in the cases where the output parameters are not mutually independent. In the context of electromagnetic levitation control, dealing with two interlinked domains, through voice coil current, i_{vc}, and relative velocity between the two masses, $\dot{z}_r$, this issue is apparent.
To tackle this problem, one possible solution is to assess the influence of each tunable parameter on the performance of the system for the specific target output based on a criteria. This task is done through the search of different parameter values within a range which is referred to as *Grid Search*. According to the system, the grid windows can be fixed intervals of linear spacing, one decade apart spacing, or randomly chosen intervals. Choosing the grid range and spacing is a pivotal task. An improper choice may create a situation where no significant change of the target output is sensed. Even in a worse case, it can cause phase shift that leads to instability. In the case of oscillatory systems, the Root Mean Square (RMS) of the output often is an appropriate metric indicating the amplitude of the overall deviation from the static equilibrium point.
Showing a high dependency on the variation of the weighting parameters of i_vc and Δu, the sensitivity analysis is conducted upon the aforementioned parameters, providing the fact that the system has no sensitivity on the remaining output variables. In Section 3.1.5, the process of the variable tuning is elaborated.

3.1.5 Optimal Parameter Selection

To find the optimal parameters for the tunable variables, despite being a straight forward method, it demands a proper grid searching of the parameters. The intervals in which the search for the optimal weights is based on, should be properly chosen. The employed method to do proper grid searching in this project is divided into two stages. The first stage uses a variable grid window that the spacing between each interval is one decade apart. Using large window size initially, facilitates the search for the zone that the optimal parameters can be found. However, bigger grid size cannot yield the exact location of the optimal solution. This sets the

motivation to conduct a secondary analysis with a smaller fixed window size in the vicinity of the optimal solution.
The benchmark for the assessment of the performance of the system is the normalized (offset) RMS of the sprung mass displacement z_s. Having known that the system oscillates about a static equilibrium point below zero, to make a fair comparison of the amplitude of oscillation, at each run, the mean value of the z_s, is subtracted from the absolute RMS value. Equation (3.13), illustrates the mathematical representation of the metric. The simulation is considered to be 10 seconds, long enough to overcome the impact of transient response. Algorithm 2, illustrates the process that the sensitivity analysis done. The algorithm holds true for both stages except for the change in weighting parameters. The simulation results are summarized in Figure 3.7.

$$RMS(z_s) = \sqrt{\frac{1}{n}\sum_{i=1}^{n}\left(z_{s_i} - \bar{z_s}\right)^2}, \quad n = T_{sample} \cdot T_{sim} \tag{3.13}$$

Grid Points	**Stage 1**		**Stage 2**	
	$w_{\Delta u}$	$w_{i_{vc}}$	$w_{\Delta u}$	$w_{i_{vc}}$
P1	0.01	0.01	0.8	17
P2	0.1	0.1	0.9	18
P3	1	1	0.95	19
P4	10	10	1	20
P5	20	20	1.05	21
P6	30	30	1.1	22
P7	50	50	1.2	23

Table 3.2: Grid search parameters of sensitivity analysis: Stage 1: Initially provides the proximity of the optimal weighting parameters. Stage 2: Yields the precise location of the optimal solution based on the results from Stage 1

Referring to Figure 3.7, according to the spectrum of the colors, the region (contour) presented in navy blue indicted the proximity of the optimal parameters using the metric $RMS(z_S)$. As can be seen, a mesh size of 70×70 along with an interpolation is done for the 3D surface, based on the the initial 7×7 data points. The same post processing with a mesh size of 100×100 is employed for the contour map. It can be roughly estimated in the region where $w_{\Delta u}$ is around 1 and $w_{i_{vc}}$ is around 20, the system has the minimum value. According to these in the second stage the value of the tuning parameters should be placed in the proximity of these values. The tuning parameters of stage 2 are enlisted in Table 3.2.

Algorithm 2 Sensitivity Analysis Algorithm

```
Define the grid elements w⃗_Δu, w⃗_ivc
Define the grid lengths L_Δu and L_ivc
for i = 1 to L_ivc do
    for k = 1 to L_Δu do
        Set MPC output variables weights = diag([0, 0, 0, 0, w_ivc(i)])
        Set MPC Manipulated variable weight = w_Δu(k)
        Simulate the model
        Extract z_s as timeseries data
        Calculate RMS(z_S)
    end for
end for
```

Following the same steps for performance assessment, in stage 2 the exact location of the optimal parameters is obtained. Eventually, the final results from sensitivity analysis yield the optimal parameters for the MPC tuning. The final results are enlisted in Section 3.1.5. Having found the optimal parameters, the performance of

Parameter	**Tuned Value**
$\dot{z}_r$	0
z_r	0
$\dot{z}_s$	0
z_s	0
i_{vc}	23
V	1
ΔV	1.2

Table 3.3: Tuned values of parameters

the control strategy is being compared to the case of passive damping.

3.1.6 MPC Optimal Performance Results with Fullstate Feedback

As depicted in Figure 3.8, fine-tuning the weighting parameters has yielded notable distinctions. Notably, there has been a 80% reduction in the amplitude of the sprung mass displacement with MPC in comparison to the passive damping setup. Similarly, there has been an approximate 55% decrease in the amplitude of the sprung mass acceleration under the same conditions. Figure 3.9, depicts

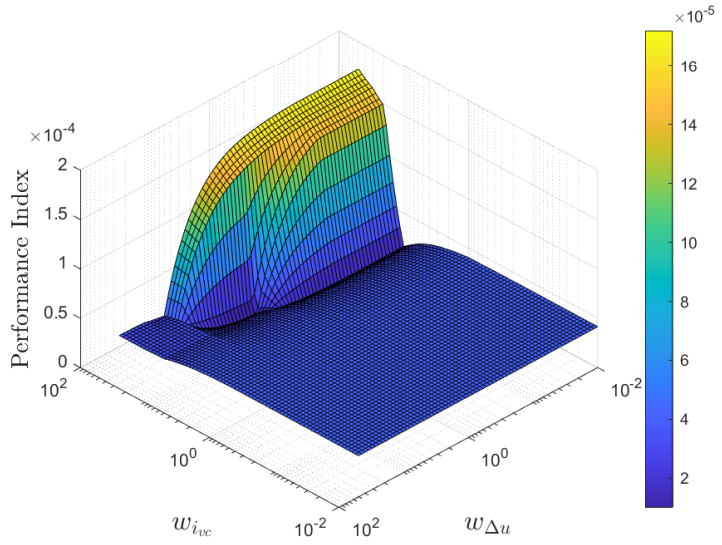

(a)

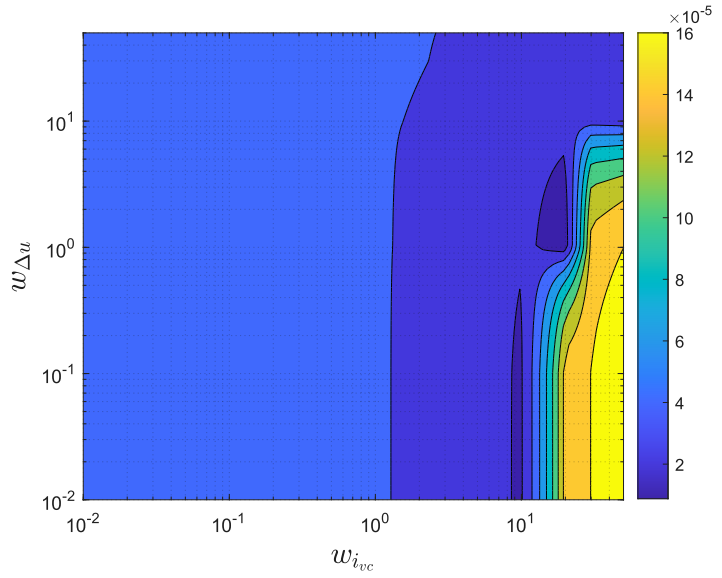

(b)

Figure 3.6: Sensitivity analysis of the tunable parameters $w_{\Delta u}$ and $w_{i_{vc}}$ in stage 1:(a) Exhibits the performance index of tuning parameters based on offset RMS values of z_s (b) Exhibits the contour map of the pertaining 3D surface

the alteration in the profile of the unsprung mass displacement under optimal control conditions. As anticipated, compared to the passive damping scenario,

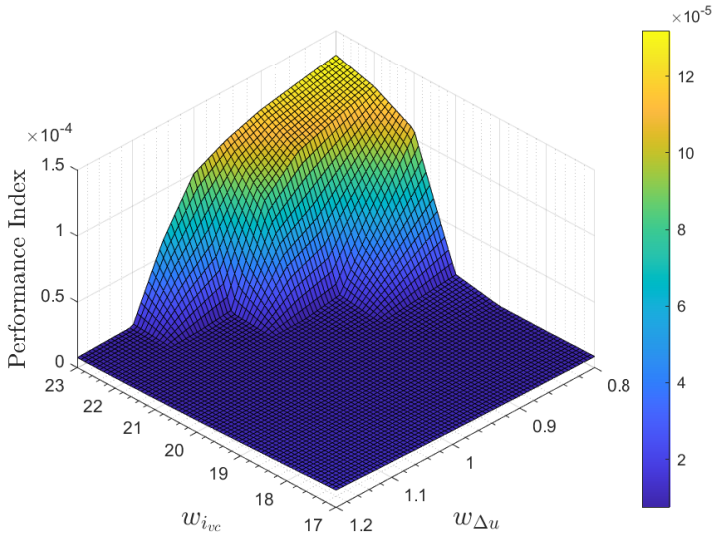

(a)

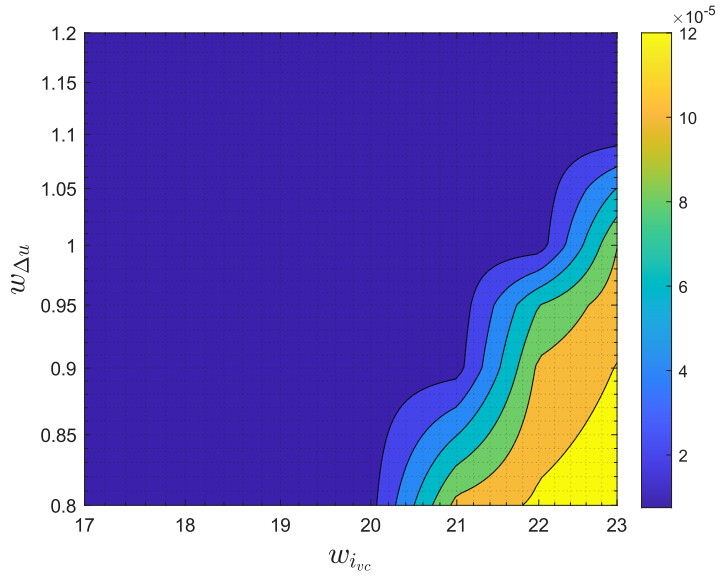

(b)

Figure 3.7: Sensitivity analysis of the tunable parameters $w_{\Delta u}$ and $w_{i_{vc}}$ in stage 2:(a) Exhibits the performance index of tuning parameters based on offset RMS values of z_s (b) Exhibits the contour map of the pertaining 3D surface

the unsprung mass demonstrates poorer performance with optimal control. This outcome arises from the track excitations primarily being absorbed by the unsprung

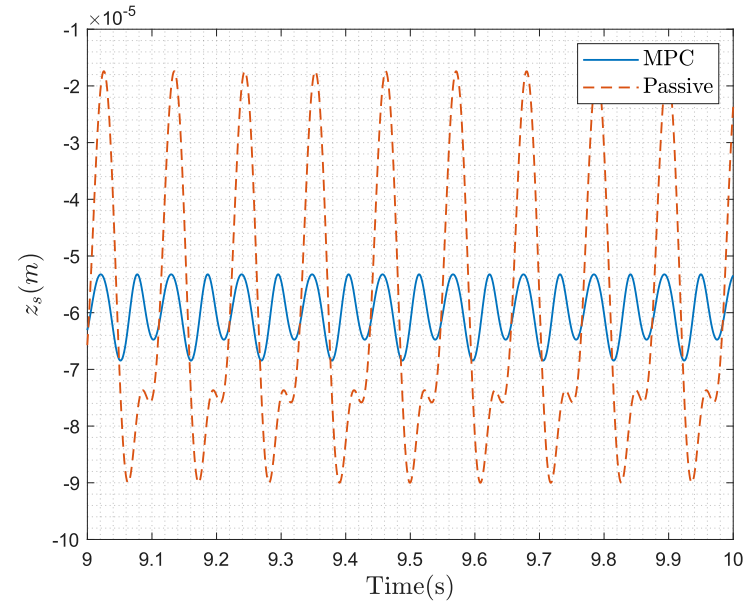

(a)

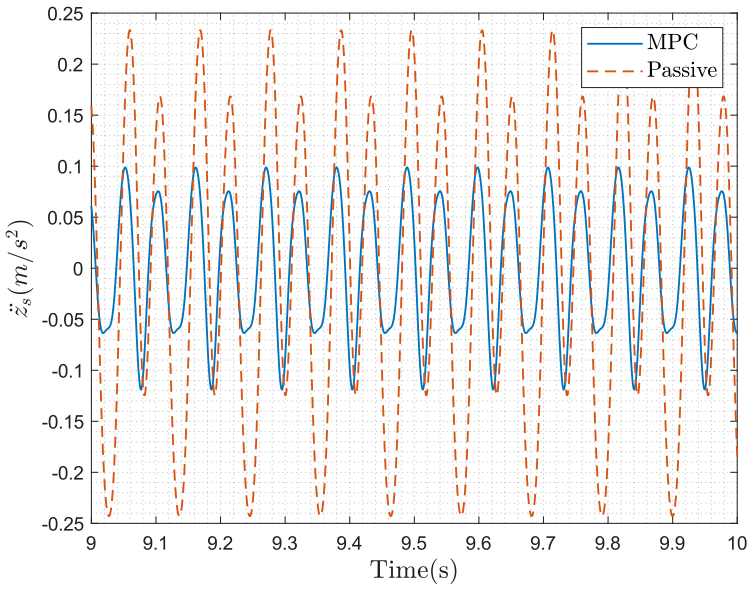

(b)

Figure 3.8: Comparison of MPC and passive damping for vibration control of sprung mass with optimal tuning of MPC: (a) sprung mass displacement comparison, z_s (b) sprung mass acceleration comparison, $\ddot{z}_s$

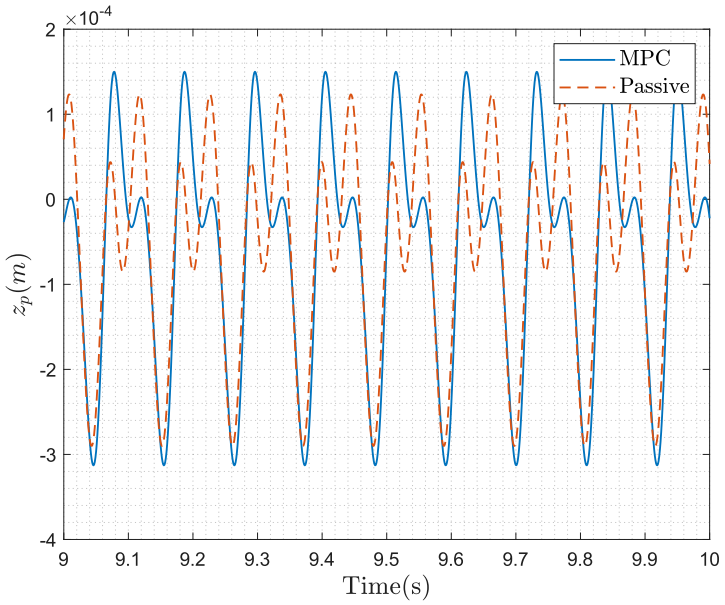

Figure 3.9: Comparison of MPC and passive damping for the displacement of unsprung mass with optimal tuning of MPC

mass. It's important to recognize that due to the unsprung mass's oscillations having an amplitude roughly 10 times greater than that of the sprung mass, even significant reductions in the displacement of the sprung mass don't notably impact the displacement of the unsprung mass.
Analyzing the forces acting on the sprung mass provides valuable insights into the system's dynamics. Specifically, in an ideal scenario, the actuation force should be equal in magnitude but 180° out of phase with the residual force, effectively canceling out the inertial force $m\ddot{z}_s$. However, in reality, there is typically a phase delay, even though the amplitudes are equal. Figure 3.10 serves as evidence supporting this assertion. It demonstrates a slight phase delay between the actuation force and the internal forces. This phase delay results in a non-zero residual force, albeit with a small enough amplitude to avoid significant accelerations. n a fully mechanical system where the source of the optimal actuation force is indifferent, the actuation and control force are typically treated as a single entity. However, in a realistic scenario like the one proposed in this project, achieving the optimal actuation force involves a medium transfer function between the control input V and the control force $u_{vc} = kmi_{vc}$. This transfer function incorporates the electrical domain equation of the VCA that is often referred to as the *internal loop*, must account for the transient phase of the input force. In other words, the optimal actuation force provided by VCA is the output of a first-order model electrical system. Consequently, there exists a further phase delay of the actuation force in

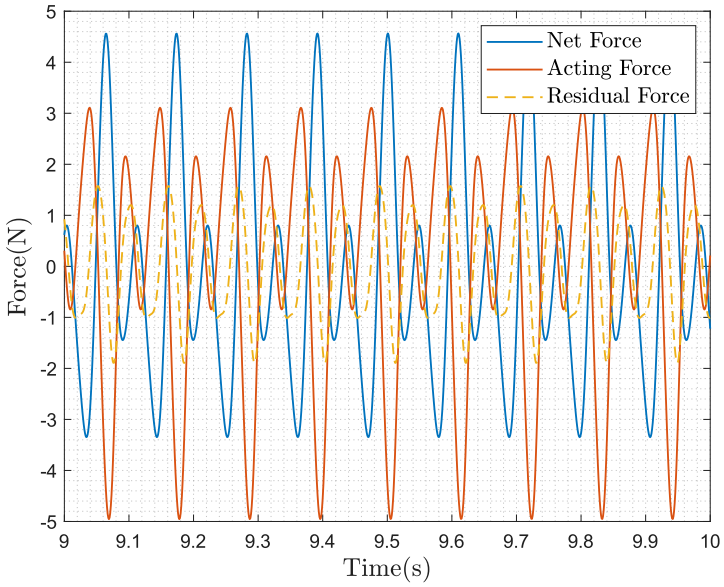

Figure 3.10: Acting forces on the sprung mass: The figure shows the sum of internal forces arising from the viscous damper and elastic spring (blue line), the actuation force coming from the VCA, $k_m i_{vc}$, (red line), and the residual force remaining in the sprung mass as the difference between the internal and actuation force (orange dashed line).

relation to the control input, which needs to be considered. This phase delay is not a concern when dealing with a fully mechanical system.
However, with the 5-state configuration integrating both electrical and mechanical domains, this issue is already addressed, and the control force is designed to be outputted as the desired actuation force. This assertion is demonstrated in Figure 3.11. To elucidate the provided force, let's convert the input voltage to force terms: F_{in} is calculated as $k_m \cdot \frac{V_{in}}{R_{vc}}$. It becomes apparent from Figure 3.11 that the actuation force $k_m i_{vc}$ exhibits a distinct profile compared to the converted input force. By comparing the sprung mass displacement z_s with the control and actuation force, it is evident that the control input is provided in a manner such that the actuation force attenuates the oscillations of z_s at each time step.

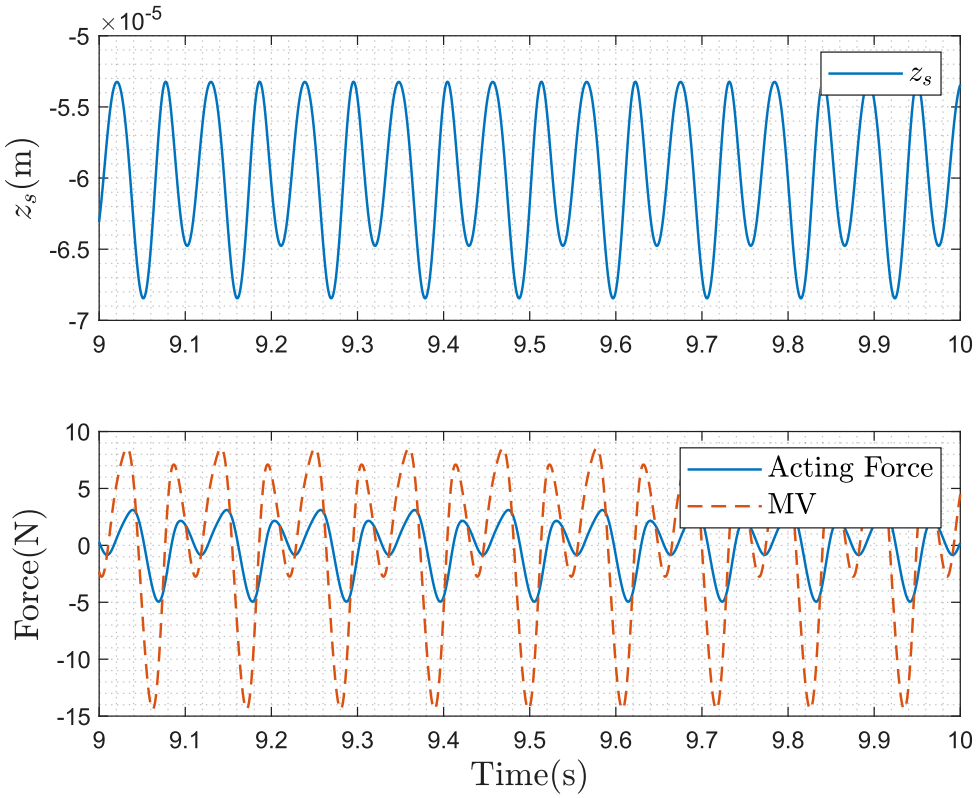

Figure 3.11: The Comparison of the effectiveness of the actuation force on the the sprung mass displacement z_s

3.1.7 MPC Performance Comparison with LQR Controller

As demonstrated, Model Predictive Control (MPC) is considered a more sophisticated iteration of the Linear Quadratic Regulator (LQR) controller, with the capability to handle constraints within the control framework. For this purpose, a comparison of performance is conducted to evaluate the performance of each controller and compare it to passive damping control.
Figure 3.12, represents the sprung mass displacement for each of the three cases. It can be observed that MPC outperforms LQR. However, when it comes to the comparison of the acceleration, as can be seen in Figure 3.13, the amplitude of the acceleration profile in MPC is slightly greater than the case with LQR control. Eventually, the comparison of the control forces are being made. Figure 3.14, represents the input forces for both MPC and LQR controller. The comparison shows that MPC uses greater force for the task of vibration isolation.

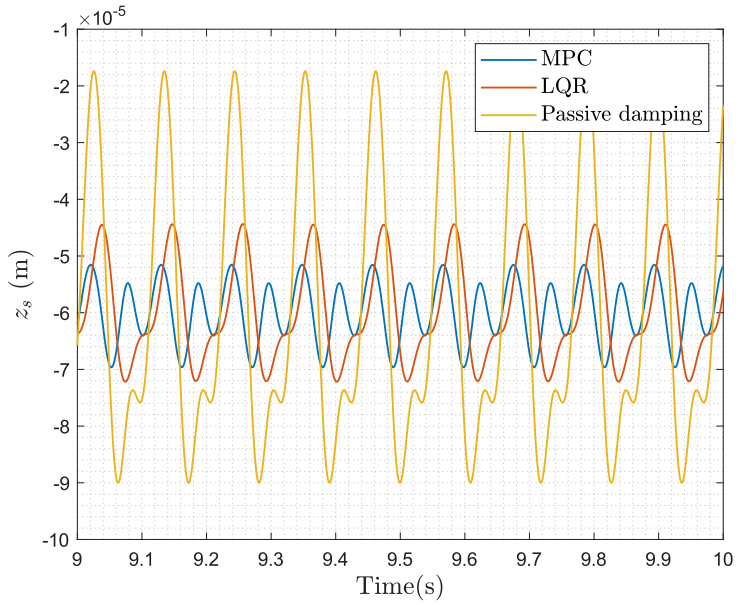

Figure 3.12: Performance comparison of MPC, LQR, and passive damping control, based on sprung mass displacement, z_s

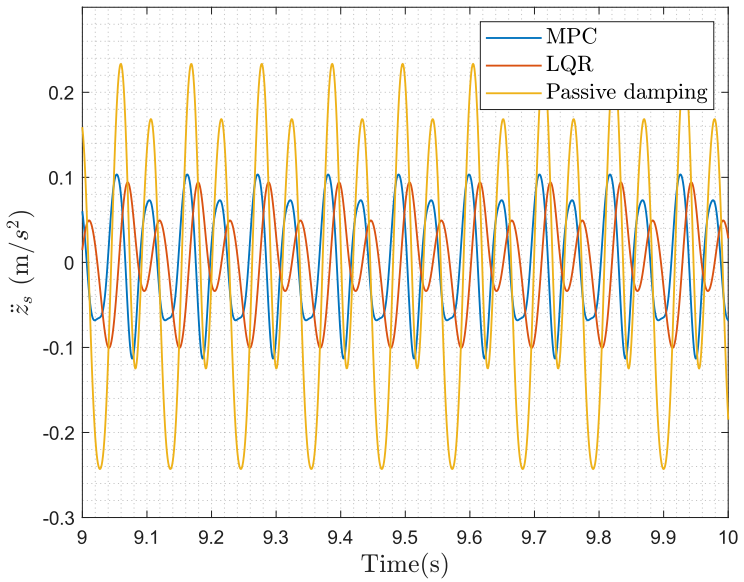

Figure 3.13: Performance comparison of MPC, LQR, and passive damping control, based on sprung mass acceleration, $\ddot{z}_s$

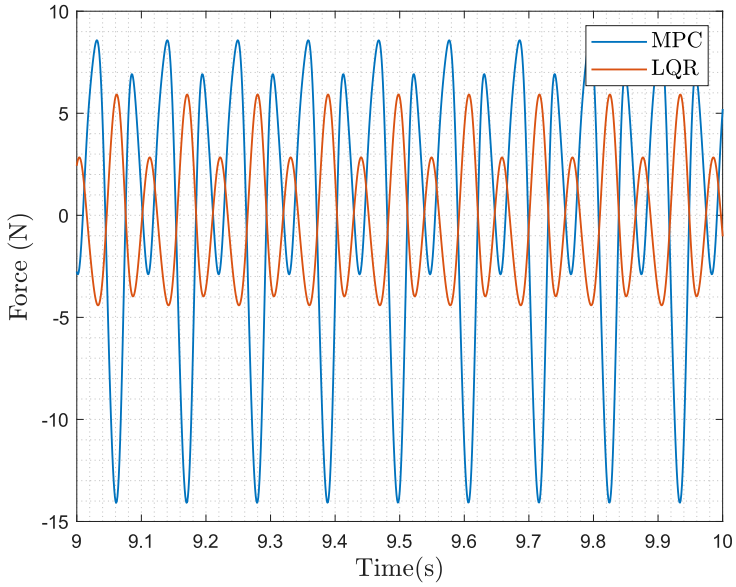

Figure 3.14: Comparison of the input force for the case of MPC and LQR controller

The comparison between the two strategies reveals that, for the purpose of passenger comfort, which depends on the sprung mass displacement and acceleration profile, the overall performance of MPC surpasses that of LQR. However, the comparison of the control forces demonstrates that LQR consumes less energy compared to MPC.

Chapter 4

State Observer

In control systems, controllers that operate based on the explicit model of the system rely on complete state feedback from the system's outputs. Model Predictive Control (MPC) similarly utilizes all system states to predict its behavior based on measured outputs. However, in practical applications, accessing all system states is often unfeasible. Sensors used to measure outputs introduce noise, resulting in imperfect measurements. Furthermore, in some cases, certain states cannot be measured at all. To address this challenge, mathematical approaches can be employed. One common strategy involves using high-pass filters to mitigate the influence of certain frequencies. These filters selectively permit frequencies below a specified cutoff frequency to pass through, effectively removing higher frequency contributions from the signal. Another set of approaches involves filters that are tailored to the specific model of the system, referred to as *State Observers*. The Kalman filter, for instance, is a prominent example of an state observer. It leverages the explicit model of the system and incorporates measurements of available states to generate refined data through estimation techniques. This enables the filter to effectively account for noise and uncertainties, yielding more accurate and reliable outputs. Indeed, the augmentation of Kalman filters takes the process a step further by estimating unmeasured quantities as well. Augmented Kalman Filters (AKF) extend the capabilities of traditional Kalman filters by incorporating additional states into the estimation process. This allows the filter to effectively handle scenarios where certain states cannot be directly measured, enhancing the overall accuracy and robustness of the filtering process.
In In this project, obtaining the relative velocity between the sprung mass and unsprung mass necessitates the use of accelerometers to capture the acceleration of these respective masses. However, converting these acceleration measurements into velocities through numerical integration introduces drift over time, primarily due to the integration of a constant term. This issue motivates the exploration

of alternative techniques for estimating relative velocity, ones that rely solely on measuring the electrical properties of the system. By doing so, the goal is to develop a method for estimating relative velocity that is not susceptible to drift and provides more reliable results. This chapter discusses the approach taken to achieve this goal.

4.1 Kalman Filter

Kalman filter (KF) was initially introduced in 1960 by Rudolf Emil Kalman, [13], marking a pivotal moment in the advancement of filtering methodologies. Unlike conventional filters, the Kalman filter operates without the constraint of assuming stationary stochastic processes for both measured signals and noise, [14]. Instead, it models the signal process as the outcome of a linear system subjected to white noise disturbances.
One of the distinctive features of the Kalman filter is its ability to deliver optimal estimation with minimal mean squared error, particularly adept at handling linear filters applied to non-stationary stochastic processes. This capability makes it exceptionally valuable in scenarios where the relationships between inputs and outputs are described by linear equations, despite the underlying stochastic processes exhibiting time-varying characteristics. By embracing this adaptive paradigm, the Kalman filter offers a robust and efficient solution, capable of navigating the complexities of dynamic systems with fluctuating uncertainties. The following section is dedicated to presenting the mathematical framework of the Kalman filter algorithm.

4.1.1 Mathematical Statement

Assuming an LTI system with the process noise of $\mathbf{w}_d$ and the measurement noise of $\mathbf{w}_n$, the states of system at time instant t, evolved from a prior state at time $t-1$, is as follows:

$$x_t = A_t x_{t-1} + B_t u_t + w_d \tag{4.1}$$
$$y_t = C_t x_t + w_n \tag{4.2}$$

The process and measurement noises are assumed to be zero mean Gaussian white noise, with covariance of Q_t and R_T, respectively.
The Kalman filter serves as a crucial tool for estimating the true state (x_t) of a system, especially when direct observation is impractical or unavailable. Instead, it leverages a combination of system models and noisy measurements to derive an estimate ($\hat{x}_t$) of the state. Importantly, these estimates are no longer discrete

values but are represented as probability density functions (pdfs), reflecting the uncertainty inherent in the estimation process.
Central to the Kalman filter's operation are Gaussian pdfs, which provide a complete description of the probability distribution. The key parameters defining these Gaussian pdfs are the variances and covariances, collectively stored in the covariance matrix P_t. Specifically, the diagonal elements of P_t correspond to the variances associated with each state variable, while the off-diagonal elements represent the covariances between different state variables.
In scenarios where the system dynamics can be accurately modeled as a one-dimensional linear system with measurement errors conforming to a zero-mean Gaussian distribution, the Kalman filter stands out as the optimal estimator. Through a recursive process, the Kalman filter equations facilitate the calculation of the updated state estimate ($\hat{x}_t$) by integrating prior knowledge, system predictions, and noisy measurements.
The Kalman filter algorithm involves two stages. The first one is the prediction stage using the model of the system. The latter being the measurement update. For the standard Kalman filter the equations defining the prediction stage are

$$\hat{x}_{t|t-1} = A_t \hat{x}_{t-1|t-1} + B_t u_t \tag{4.3}$$
$$P_{t|t-1} = A_t P_{t-1|t-1} A_t^T + Q_t \tag{4.4}$$

The variance associated with the prediction $\hat{x}_{t|t-1}$ of an unknown true value x_t is given by Equation (4.5)

$$P_{t|t-1} = \mathbb{E}[(x_t - \hat{x}_{t|t-1})(x_t - \hat{x}_{t|t-1})^T] \tag{4.5}$$

where $\mathbb{E}[.]$ denotes the expectation operator.
Noting the fact that state estimation errors and process noise have no correlation, one can obtain the following relation .

$$P_{t|t-1} = A P_{t-1|t-1} A^T + Q_t \tag{4.6}$$

Furthermore, the measurement update equations are given by

$$\hat{x}_{t|t} = \hat{x}_{t|t-1} + K_t(y_t - C_t \hat{x}_{t|t-1}) \tag{4.7}$$
$$P_{t|t} = P_{t|t-1} - K_t C_t P_{t|t-1} \tag{4.8}$$

where

$$K_t = P_{t|t-1} C_t^T (C_t P_{t|t-1} C_t^T + R_t)^{-}1 \tag{4.9}$$

It is possible to mathematically represent the aforementioned equations using the Gaussian pdfs. In this case for a given state, r, the prediction and measurement

update stages are defined as following

$$f_1(r;\mu_1,\sigma_1^2) = \frac{1}{\sqrt{2\pi\sigma_1^2}} \exp\left(-\frac{(r-\mu_1)^2}{2\sigma_1^2}\right) \tag{4.10}$$

$$f_2(r;\mu_2,\sigma_2^2) = \frac{1}{\sqrt{2\pi\sigma_2^2}} \exp\left(-\frac{(r-\mu_2)^2}{2\sigma_2^2}\right) \tag{4.11}$$

The state estimation in the Kalman filter involves fusing two probability density functions (pdfs) by multiplication. It's noteworthy that the fused model remains a Gaussian PDF. This aspect is pivotal because it facilitates the multiplication of an infinite number of Gaussian pdfs over time without escalating the complexity or the number of terms in the resultant function. With each time epoch, the new pdf continues to be fully represented by a Gaussian function. This inherent property underscores the elegant recursive nature of the Kalman filter [15].The fusion model that is the product of two pdfs is given by

$$f(r;\mu_{\text{fused}},\sigma_{\text{fused}}^2) = \frac{1}{\sqrt{2\pi\sigma_{\text{fused}}^2}} \exp\left(-\frac{(r-\mu_{\text{fused}})^2}{2\sigma_{\text{fused}}^2}\right) \tag{4.12}$$

where

$$\mu_{\text{fused}} = \frac{\mu_1{\sigma_2}^2 + \mu_2{\sigma_1}^2}{{\sigma_1}^2 + {\sigma_2}^2} \tag{4.13}$$

and

$$\sigma_{\text{fused}} = \frac{\sigma_1^2\sigma_2^2}{\sigma_1^2 + \sigma_2^2}. \tag{4.14}$$

The graphical representation of the Equations (4.10) to (4.12), is illustrated in Figure 4.1.

To enable the multiplication of prediction and measurement pdfs, it's necessary to transform one into the domain of the other. A common approach is to map predictions into the measurement domain using the transformation matrix C_t. This matrix facilitates the conversion of predicted states into measurements, aligning them in the same domain for comparison and fusion. This practice ensures that both prediction and measurement pdfs are represented in a common space, allowing for meaningful combination and estimation within the Kalman filter framework. After the domain adaptation the converted relations are as following

$$\mu_{\text{fused}} = \mu_1 + K \cdot (\mu_2 - C\mu_1) \tag{4.15}$$

$$\sigma_{\text{fused}}^2 = \sigma_1^2 - KC\sigma_1^2 \tag{4.16}$$

where

$$K = \frac{C\sigma_1^2}{C^2\sigma_1^2 + \sigma_2^2} \tag{4.17}$$

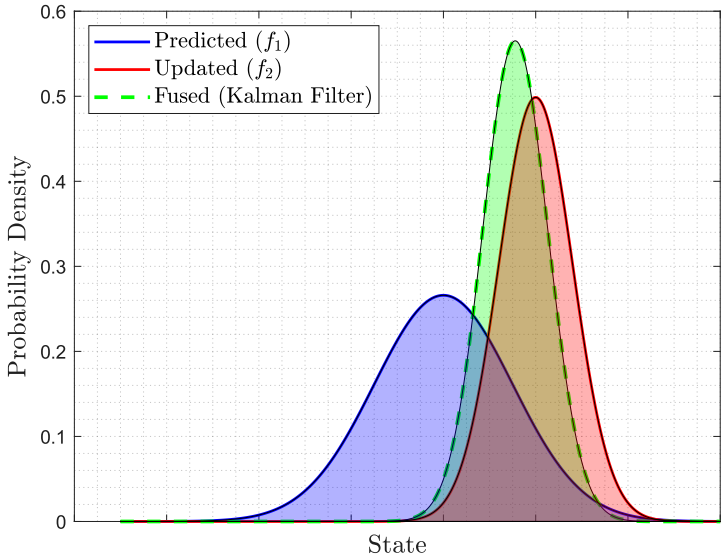

Figure 4.1: Probability density functions associated with the prediction (blue), measurement update (red), and the fusion (green) stages of Kalman filter algorithm for an individual state

Certain terms resulting from this scalar derivation can now be compared with the standard vectors and matrices used in the Kalman filter algorithm.

- $\mu_{\text{fused}} \rightarrow \hat{x}_{t|t}$: the state vector estimated using fusion data
- $\mu_1 \rightarrow \hat{x}_{t|t-1}$: state vector predicted prior to data fusion
- $\sigma^2_{\text{fused}} \rightarrow P_{t|t}$: covariance matrix associated with the data fusion
- $\sigma^2_{\text{fused}} \rightarrow P_{t|t-1}$: covariance matrix associated prior to the data fusion
- $\mu_2 \rightarrow y_t$: vector of measurements (outputs)
- $\sigma^2_2 \rightarrow R_t$: the uncertainty matrix associated with a noisy set of measurements
- C: the transformation matrix mapping the states to the outputs

Using the analogy between the scalar and multi-state domains one can move from the scalar relations, Equations (4.3) and (4.9) to the vectorial relations in Equations (4.15) and (4.17).

4.1.2 Augmented Kalman Filter

In the context of state observing, the Augmented Kalman Filter (AKF) extends the classic Kalman filter framework by incorporating additional state variables, known as augmented states, into the estimation process [16]. These augmented states represent unobservable quantities or dynamics that influence the system's behavior but cannot be directly measured. By augmenting the state vector with these additional variables, the AKF enables the estimation of both observable and unobservable states, resulting in more accurate and comprehensive state estimation.
Considering an LTI system with outputs depending only on states (no direct feedthrough), a full-state estimator is a dynamic system designed to generate an estimate $\hat{x}$ for the full state x solely based on the information derived from noisy sensor measurements y, actuation input u, and a model representing the dynamics of the process [17]. In a continuous time domain analogous to Equations (4.1) and (4.2), the estimates states can be defined given by

$$\dot{\hat{x}} = A\hat{x} + Bu + K_f(y - \hat{y}) \tag{4.18}$$
$$\hat{y} = C\hat{x} \tag{4.19}$$

$$\dot{x} = (A - K_f C)\hat{x} + [Kf \quad B] \begin{bmatrix} y \\ u \end{bmatrix} \tag{4.20}$$

For observable systems, it is possible to arbitrarily position the eigenvalues of the estimator dynamics $A - K_f C$, resulting in stable convergence of the estimate $\hat{x}$ to the true state x. To demonstrate that stable dynamics $A - K_f C$ lead to a stable estimator that converges to the full-state x, consider the time dynamics of the estimation error $\varepsilon = x - \hat{x}$. In this case one can show the following relation

$$\frac{d}{dt}(\varepsilon) = (A - K_f C)\varepsilon + w_d - K_f w_n \tag{4.21}$$

Therefore, as long as $A - K_f C$ is stable, the estimate $\hat{x}$ will converge to the true state x. Similar to the scenario in Linear Quadratic Regulator (LQR), there exists a trade-off between over-stabilization and the amplification of noise.
The Kalman filter, serving as an optimal full-state estimator, aims to minimize the following cost function:

$$J = \lim_{t \to \infty} \mathbb{E}\left[(x_t - \hat{x})(x_t - \hat{x})^T\right] \tag{4.22}$$

Implicitly encoded within this cost function are the noise and disturbance covariances, crucial for determining the optimal balance between aggressive estimation and noise attenuation. The mathematical derivation of an optimal solution closely

parallels that of LQR. Consequently, this problem is often referred to as linear quadratic estimation (LQE) due to its dual formulation. Like wise to the classic Kalman, the optimal Kalman filter gain K_f for an augmented system is obtained through the solution of the algebraic Riccati equation stated in Equation (4.9). In Figure 4.2, the working principle of the augmented Kalman filter is illustrated. As can be seen the observer is fed with measured states of the plant along with the inputs given to the system.

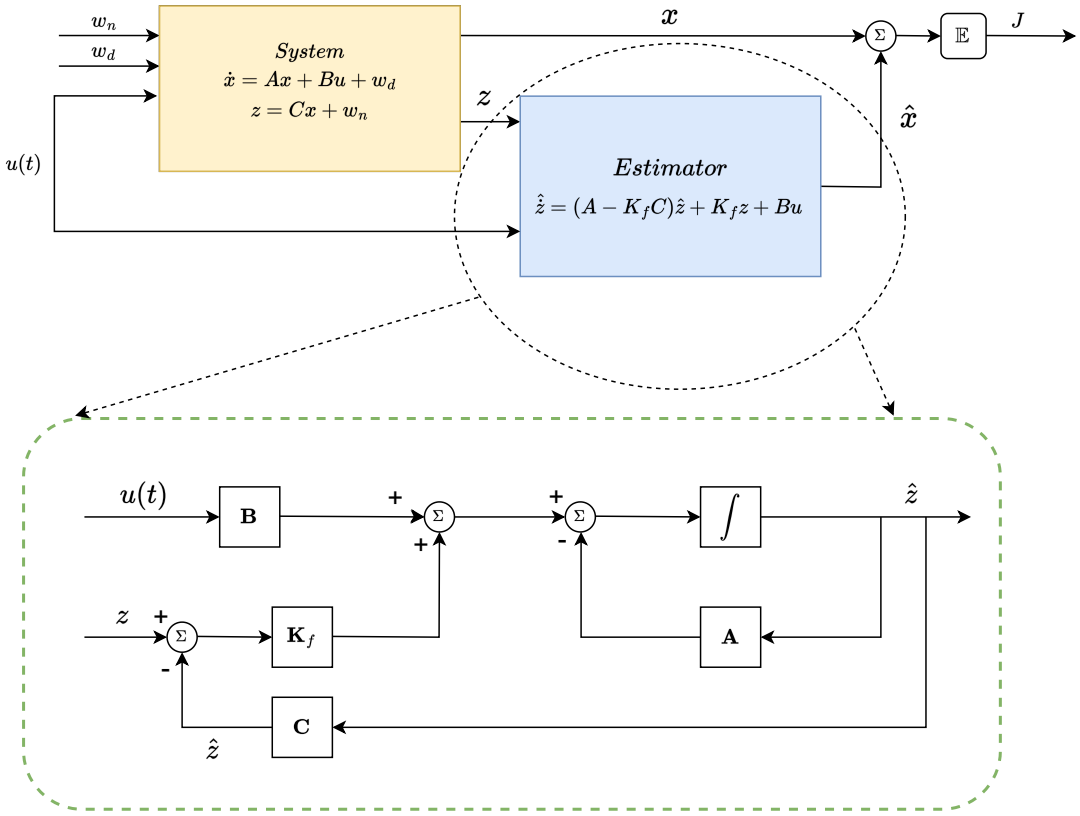

Figure 4.2: Closed loop feedback control of a generic LTI system scheme augmented with state estimator: $\hat{x}$ and x denote the estimated states and real states, and $\hat{z}$ and z represent the estimated outputs and measured outputs.

4.2 Relative velocity Estimation

The state vector described in Appendix A.4 encompasses four mechanical states represented in terms of velocity and displacement, along with one electrical property, namely current. However, measuring mechanical quantities presents challenges. Direct measurement of displacement and velocity using optical sensors can be unreliable, especially in systems with high oscillation frequencies. In such cases, accelerometers offer a more reliable solution with easy installation and high reliability. Yet, deriving velocity and displacement from acceleration data requires integration over time, which can introduce errors, particularly when employing numerical techniques in discrete time domains. Additionally, integration constants may lead to drift in computed integrated quantities. On the contrary, measuring electrical quantities like voltage and current is comparatively easier and offers high accuracy to a significant extent. Moreover, the interconnection between the electrical and mechanical domains via the definition of back electromotive force (emf), which involves relative velocity, serves as the primary motivation in this project to estimate $\dot{z}_r$ through the measurement of electrical quantities.

4.2.1 Estimation Model

The mathematical model employed to provide the estimation of relative velocity $\dot{z}_r$, is the electrical model presented in Section 2.1.2 through Equation (2.7). In this model the resistance of the VCA is considered to be constant[1]. Using the canonical form of the Equation (2.7), being the derivative of the VCA current in the left side of the equation yields

$$\frac{d}{dt}i_{vc} = (\frac{1}{L_{vc}})V - (\frac{R_{vc}}{L_{vc}})i_{vc} - (\frac{1}{L_{vc}})E_{vc} \tag{4.23}$$

This method's drawback lies in utilizing the derivative of the measured current, leading to the introduction of noise in the calculated back-EMF signal. Employing this signal as a feedback variable for active damping control could lead to less-than-optimal vibration attenuation,[8]. As a result, a disturbance observer, based on the Kalman filter, is developed to mitigate model parameter uncertainty and external disturbance signals, as illustrated in Figure 4.3. Assuming the induced voltage E_{vc} acts as a disturbance with a zero derivative [18], the following expression can be formulated:

$$\frac{d}{dt}E_{vc} = 0 \tag{4.24}$$

The derivative of the back-EMF tends towards zero due to the assumption that the

[1]Considering a constant resistance for the VCA model will results in a drift in the estimation of the relative velocity. This issue is addressed in Section 4.2.4.

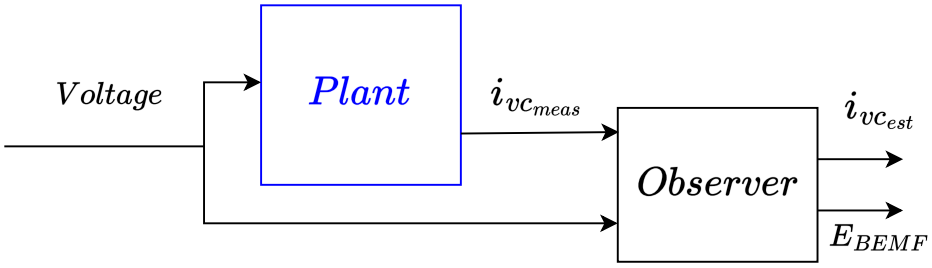

Figure 4.3: State observer model for the estimation of relative velocity through estimation of induced voltage, E_{vc}

relative velocity variation caused by the mechanical dynamics of the electrodynamic levitation system is slower than the electrical dynamics of the VCA. Consequently, the induced voltage, intertwined with the relative velocity variable via the VCA velocity constant K_v, exhibits quasi-static behavior [8]. Fusing Equation (4.23) and Equation (4.24), the continuous state space model of the estimation model is as follows

$$\frac{d\eta}{dt} = A_{\text{vc}}\eta + B_{\text{vc}}u \tag{4.25}$$

$$y = C_{\text{vc}}\eta \tag{4.26}$$

Where

$$\eta = \{i_{vc} \quad E_{vc}\}^T \tag{4.27}$$

$$u = \{V\} \tag{4.28}$$

$$y = \{i_v c\} \tag{4.29}$$

$$A_{vc} = \begin{bmatrix} \frac{-R_{vc}}{L_{vc}} & \frac{-1}{L_{vc}} \\ 0 & 0 \end{bmatrix} \tag{4.30}$$

$$B_{vc} = \{\frac{-1}{L_{vc}} \quad 0\}^T \tag{4.31}$$

$$C_{vc} = [1 \quad 0] \tag{4.32}$$

$$D = [0]. \tag{4.33}$$

The augmented plant model that is employed in the observer, is obtained using the generic AKF model described in Equation (4.20). The new augmented model holds the same stats as the one indicated in Equation (4.30). For the augmented model following the same notation as in Equation (4.30) and Equation (4.3), the

estimated states are being denoted with $\hat{\eta}$. The new input matrix is augmented with the measured outputs, namely, the voice coil current, i_{vc}. Eventually, both state are considered as the outputs of the observer using and identity matrix for the transition matrix C_{aug}. As a result the state space model of the augmented system is given by

$$\frac{d\hat{\eta}}{dt} = A_{\text{aug}}\hat{\eta} + B_{\text{aug}}\bar{u} \tag{4.34}$$

$$y_{aug} = C_{\text{aug}}\hat{\eta} \tag{4.35}$$

where

$$\hat{\eta} = \{\hat{i}_{vc} \quad \hat{E}_{vc}\}^T \tag{4.36}$$

$$\bar{u} = \{V \quad i_{vc}\} \tag{4.37}$$

$$y_{aug} = \{\hat{i}_v c \quad \hat{E}_{vc}\} \tag{4.38}$$

$$A_{aug} = A_{vc} - K_f C_{vc} \tag{4.39}$$

$$B_{aug} = \{B_{vc} \quad K_f\}^T \tag{4.40}$$

$$C_{vc} = \begin{bmatrix} 1 & 0 \\ 0 & 1 \end{bmatrix} \tag{4.41}$$

$$D = \begin{bmatrix} 0 & 0 \\ 0 & 0 \end{bmatrix}. \tag{4.42}$$

Noise pertaining to both states and measurements is taken into account within the covariance matrices Q and R, where they serve as adjustment parameters.

$$Q = \begin{bmatrix} w_i^2 & 0 \\ 0 & w_E^2 \end{bmatrix} \quad \text{and} \quad R = v_i^2 \tag{4.43}$$

where, the weighting parameter w_i pertains to noise affecting the estimated current, while v_i accounts for noise in the measured current. Parameter w_E addresses noise related to the back-EMF. The numerical parameters of the KAlman filter are enlisted in Table 4.1.[2]

4.2.2 Data Acquisition Setup

To evaluate the performance of the designed Kalman filter in estimating relative velocity, a dedicated data acquisition setup has been developed to collect experimental results from the testbench. Data acquisition setup (DSA), is designed to

[2]The value of the resistance is initially considered to be 1.65 Ohms. The true value of the resistance must be tuned after the data acquisition.

Parameter	Value
R_{vc}	1.65 Ω
L_{vc}	0.0152 H
K_v	25 Vs/m
w_i	0.001 A
w_E	0.0075 V
v_i	0.001 A

Table 4.1: Kalman filter parameters

acquire the estimated velocity and current in real-time to visually compare with that of the simulated results. The setup can be broken down into hardware and software setup. Figure 4.4, illustrates the data acquisition setup (DSA) that is used in the project. As shown in Figure 4.4, the testbench is controlled by two PCs.

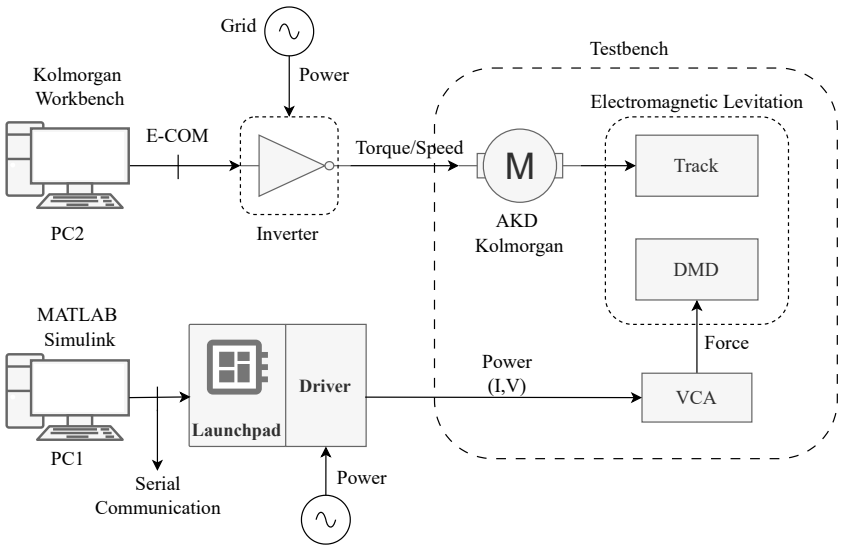

Figure 4.4: Hardware setup for the data acquisition from testbench

The first computer having the estimator and the plant model, is used to provide the offset voltage command, acquire the measured data, namely the VCA current, and provide the estimated back-emf. These commands are transfered through a serial communication to the launchpad. The launchpad is a LAUNCHXL-F28379D

The first PC serves as the host , that is using Matlab Simulink to provide the commands to the launchpad. A Matlab Simulink file that has the estimator model is provided for this purpose. Through serial communication the commands are

transferred to LAUNCHXL-F28379D microcontroller, Figure 4.5. The LAUNCHXL-F28379D is a microcontroller development kit designed by Texas Instruments. It features the TMS320F28379D microcontroller, which belongs to the C2000 Delfino series. This microcontroller is based on the high-performance, floating-point Delfino core, making it well-suited for real-time control applications. It offers various peripherals and interfaces, including analog-to-digital converters (ADCs), pulse-width modulation (PWM) modules, and serial communication interfaces (such as UART, SPI, and I2C). The control commands become amplified through the driver that is hardwired to a power supply to deliver electrical power to the VCA.

The secondary computer is tasked with overseeing the operation of the actuation

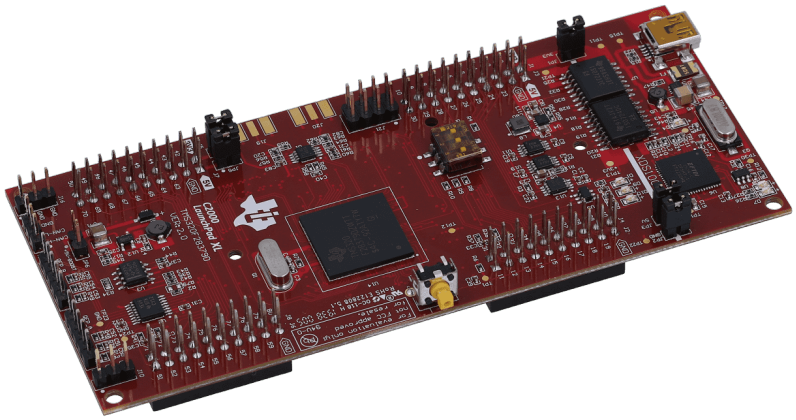

Figure 4.5: Detailed view of the LAUNCHXL-F28379D microcontroller

motor responsible for manipulating the copper track. It is responsible for defining the desired acceleration and deceleration rates of the motor, as well as setting the target angular velocity. To achieve this, the Kolmorgan Workbench software is utilized. This software enables users to regulate the motor's performance parameters by providing power and generating torque through an inverter powered by an electrical source from the grid.

In addition to the physical setup introduced earlier, there is the software component managed within PC1. As illustrated in Figure 4.6, PC1 serves as the core of the system, transmitting the input voltage signal to the estimator. A pulse width modulation (PWM) module is utilized to set the duty cycles of the system. Analog signals representing the measured current are converted into digital bits using an analog-to-digital converter (ADC). For updating resistance values, a clock mechanism provides the necessary indexing parameter for the updated state space model of the estimator. Eventually the scale factor K_v, converts the estimated E_{vc}

to the relative velocity.

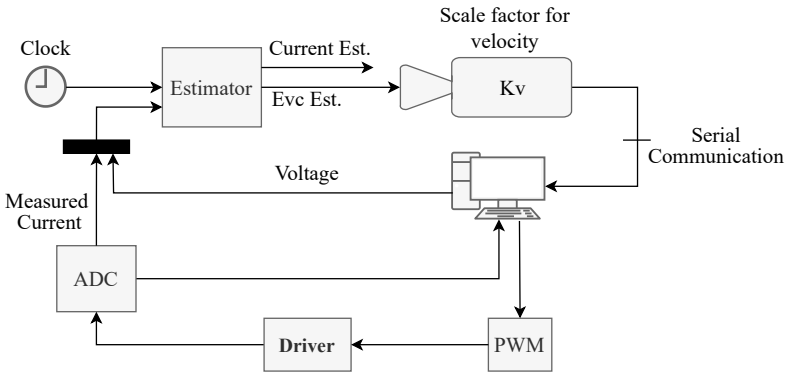

Figure 4.6: Software setup for the data acquisition from testbench

4.2.3 Experimental Results Considering a Constant VCA Resistance ($\mathbf{R_{vc} = cte}$)

Considering the resistance as a constant parameter, the estimation of the back-EMF is tested using the experimental setup. The test is conducted at constant disk angular velocity of 500 RPM. The masses are positioned on the micrometric stage such that any pre-deformation of the flex hinges are prevented. To decouple the two masses, an offset voltage of 10 volts is applied, creating a force to oppose the static force due to the the mass of the sprung mass. The results from real-time estimation of $\dot{z}_r$ and i_{vc} are being compared with the numerical simulations.

Referring to Figures 4.7 and 4.8, for an 80 second run of the testbench the comparison between the experimental results from the relative velocity and that of the model simulation are being compared. The comparison between the simulated and the estimated i_{vc} in Figure 4.7, displays a mismatch as opposed to the expectation. According to the simulation, VCA current oscillates about a constant value of approximately 7A that the constant term is due to the offset voltage applied to keep the two masses separated. Accordingly, the periodic portion of the current corresponds to the excitations coming from the copper track irregularities. On the other hand, the acquired data from the experimental test displays a different behaviour. The discrimination between the simulation and the experimental results can be divided into two components. The first one is the initial deviation from the simulated quantity. As can be seen in Figure 4.7, the experimental current initially starts below the expected current. Disregarding the transient response of the electrical domain due to the inductive component, L_{vc}, the relation, $V = R_{vc}Ivc$ not precise enough but roughly can showcase the relation between the input voltage V and the output current, i_{vc}.

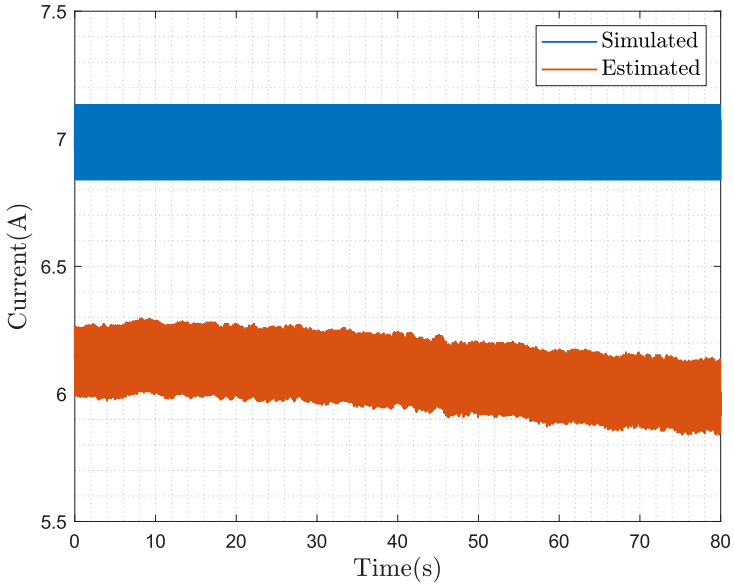

(a)

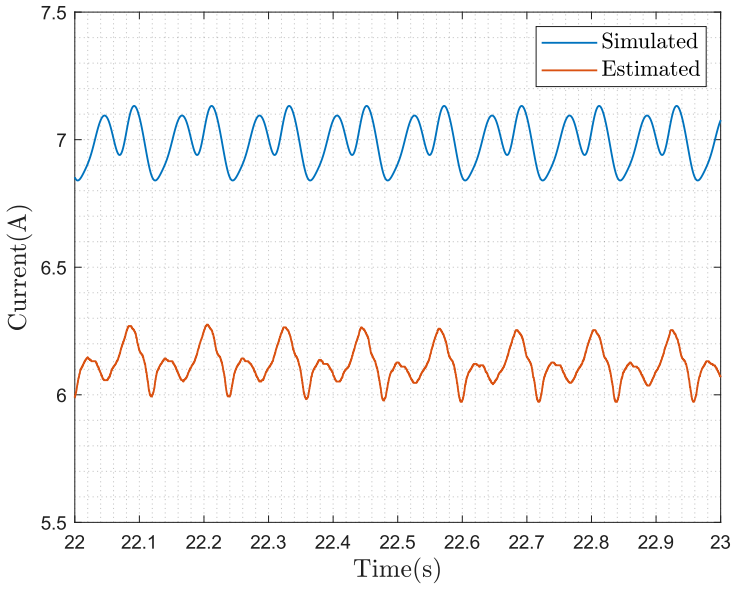

(b)

Figure 4.7: VCA Current comparison between the simulation and Kalman filter estimation from experimental data: (a) the time interval is considered to be 80 seconds to showcase the general profile of the relative velocity (drift) (b) zoomed view

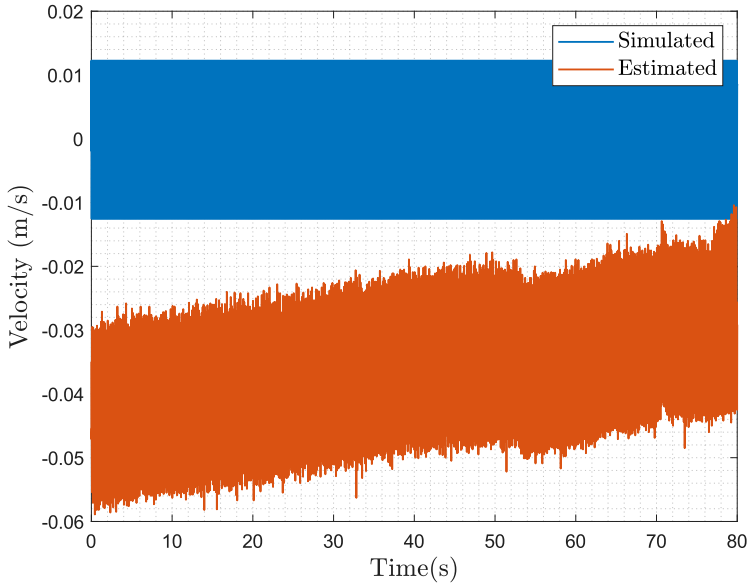

(a)

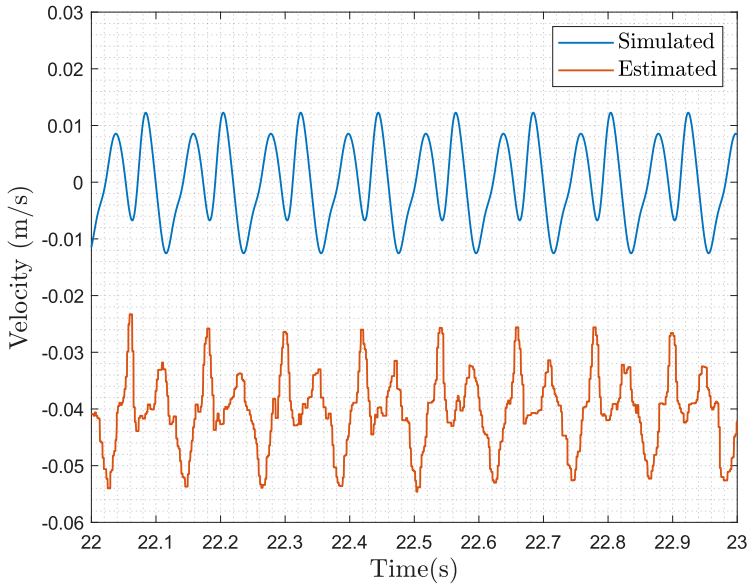

(b)

Figure 4.8: Relative velocity comparison between the simulation and Kalman filter estimation from experimental data: (a) the time interval is considered to be 80 seconds to showcase the general profile of the relative velocity (drift) (b) zoomed view

Knowing the fact that the applied voltage is constant of 10 volts, the smaller initial value of i_{vc} indicated that the hypothesized initial value for R_{vc} is larger than the actual VCA resistance. Due to the same reason the estimated relative velocity as well has an initial offset with respect to the expected zero relative velocity from the numerical model, Figure 4.8. To address this issue by means of trial and error the estimation model is retuned to a value of $R_{vc} = 1.485\ \Omega$. Figure 4.9 represents the case with retuned value of R_{vc}.
Retuning the resistance solves the issue of initial mismatch, however, for a long period of time the results from the experimental tests show that even with a refined resistance value the profile of the VCa current drifts downwards with respect to the simulation in time and accordingly the profile of the estimated velocity drifts upwards. This issue is associated with the physical properties of the VCA. Applying a constant voltage and letting a constant current run through the terminals of the VCA, generates heat with respect to time. The resistance of R_{vc}, increases as the temperature goes up. This continuous increment in resistance results in a continuous reduction in the flow of the current that is evident in Figure 4.7. This phenomenon is in contrast with the initial hypothesis that the resistance coefficient in Equations (2.7) and (4.23) is considered to be constant, i.e. that model representing the electrical domain of the system is not LTI. To address this issue a novel technique is employed that is based on the offline update of the resistance with respect time.

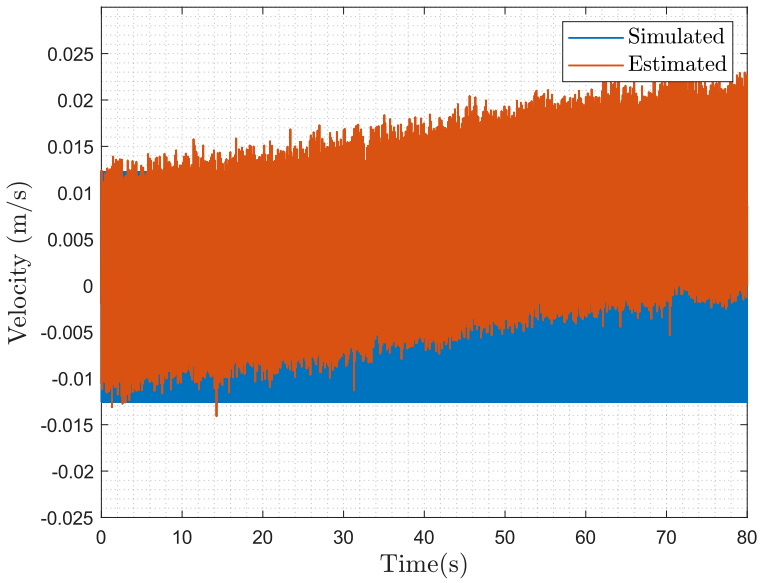

(a)

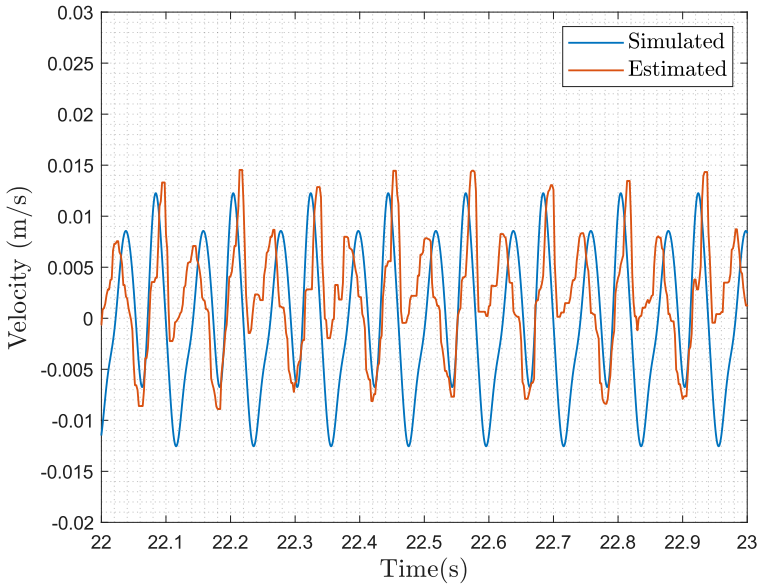

(b)

Figure 4.9: Relative velocity comparison between the simulation and Kalman filter estimation from experimental data with retuned VCA resistance ($R_{vc} = 1.485\Omega$): (a) the time interval is considered to be 80 seconds to showcase the general profile of the relative velocity (drift) (b) one second snapshot of (a) for profile comparison

4.2.4 Estimation Model with Offline Resistance Update, $\mathbf{R_{vc} = R_{vc}(t)}$

To address the challenge of drift in estimating relative velocity, it's crucial to examine the rise in resistance observed during testing. As mentioned the reason why the resistance increase is linked with the rise in the temperature of the resistance due to the constant passage of current through coil. To showcase this an approximated function of the resistance with respect to the time is drawn by dividing the input voltage by the measured current. It is obvious that the contribution of the inductive component and the the back-emf make it less precise to use such relation ($R = \frac{V}{i}$), however, it is still a useful tool to represent the approximate behaviour of the resistance. Referring to the results from the first test that are presented in Figure 4.7, and approximate resistance is obtained. In order to have a more clear representation of the data, they are being further post-processed by means of a moving average filter and reported in Figure 4.10. According to

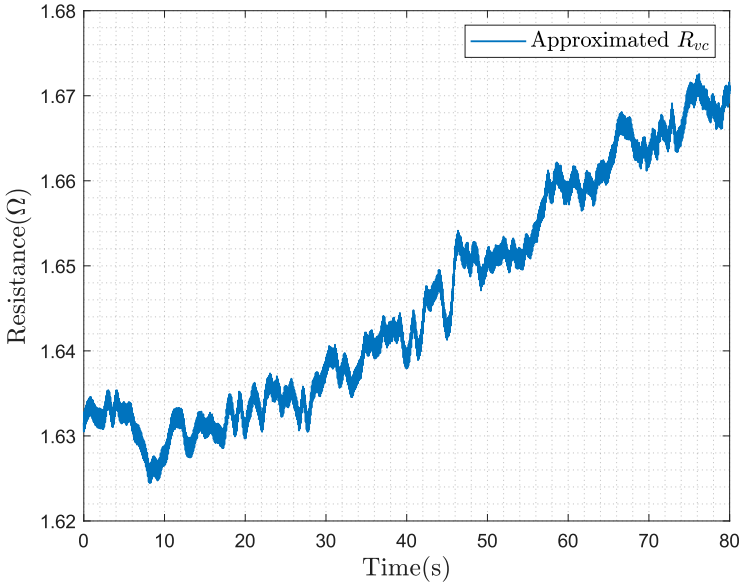

Figure 4.10: Approximated resistance of the VCA coil using the relation $R = \frac{V}{I}$

Figure 4.10, the profile of the resistance exhibits a linear growth. Moreover, the slope of the graph using a linear interpolator ($m = \frac{R_f - R_i}{\Delta t}$), is 0.0005 Ω/s. Although for longer runs of the track this assumption might not hold true but for shorter periods (less than 5 minutes) this assumption is sufficiently accurate. Being a pivotal factor in the estimation the relative velocity, the resistance change must be taken into account in the equation of the VCA. Mathematically speaking, the term R_{vc} in Equation (4.23) must become a linear function of time. Substituting

$R_{vc} = mt + R_0$ into Equation (4.23), one can get

$$\frac{d}{dt}i_{vc} = \left(\frac{1}{L_{vc}}\right)V - \left(\frac{mt + R_0}{L_{vc}}\right)i_{vc} - \left(\frac{1}{L_{vc}}\right)E_{vc} \tag{4.44}$$

where R_0 is the initial resistance of the resistor and m is the slope of the growth. Having a time dependant component in the state matrix means that the system of equations are no more time invariant. Solving Equation (4.44) for i_{vc}, demands the integrating factor $\mu(t) = e^{\int(\frac{mt+R_0}{L_{vc}})dt}$ that is depending on time. In this case one can write the state space equations of the VCA in the following form.

$$\dot{x}(t) = A(\rho(t))x(t) + B(\rho(t))u(t) \tag{4.45}$$
$$y(t) = C(\rho(t))x(t) + D(\rho(t))u(t) \tag{4.46}$$

where $x(t) \in \mathbb{R}^n$ is the state vector, $u(t) \in \mathbb{R}^m$ is the input vector, $y(t) \in \mathbb{R}^p$ is the output vector, $\rho(t) \in \mathbb{R}^q$ is the varying parameter vector, and $A(\rho(t))$, $B(\rho(t))$, $C(\rho(t))$, and $D(\rho(t))$ are matrices or functions that depend on the varying parameter $\rho(t)$. The system of state space equations Equations (4.45) and (4.46) is referred to as *Linear Parameter Varying* (LPV) systems as the physical properties of the system depend on a particular parameter.
The solution of such equations is often analytically impossible. However, numerically speaking, one can regard an LPV system as discrete LTI systems that each LTI depends on the instantaneous value of $\rho(t)$ and the general model is an interpolation of the individual LTI systems within the domain. This feature allows for considering the changes in the resistance of the VCA. However, as discussed, the augmented Kalman filter uses the LTI model of the system to estimate back-emf. The provided Kalman gain as well is a constant vector that only depends on the constant state, input and transition matrix entries. For this reason the model must be updated according to the update of resistance in the Kalman filter. However, as LQR approach is used to obtain the gain vector based on a cost function, during the online test the online update of the model for Kalman filter in real-time might encounter computational problems due to microprocessor CPU limitations. To overcome this issue, a novel approach is introduced that is based on the offline update of the Kalman gain. To abbreviate the notation AKFVG is used in substitute with augmented Kalman filter with variable gain and AKFCG is used to denote augmented Kalman filter with constant gain. In this method, considering that the dynamic of system change significant enough to cause drift in Δt seconds, a democratization sampling time is chosen that is equal to this interval, $T_s = \Delta t$. During this period, similar to the previous case the Kalman gain is obtained for the specific resistance, $R_{vc}^{\Delta t_i}$. For the consecutive sampling interval, the same process is conducted except for an updated resistance,$R_{vc}^{\Delta t_{i+1}} = R_{vc}^{\Delta t_i} + m\Delta t_i$. Once all the

LTI state space models are obtained for a predefined test period, using the nearest neighbors method, all the individual models are interpolated yielding the final LPV model. This offline method allows for the the estimator to select the associated LTI model based on an indexing parameter that is referred to as *scheduling parameter*. Algorithm 3, demonstrates the functioning of the aforementioned method. The

Algorithm 3 Updated augmented Kalman gain algorithm

Initialize the slope of resistance, $m_{R_{vc}}$
Initialize a 3D matrix for augmented state spaces $(A^{\Delta t_i}, B^{\Delta t_i}, C^{\Delta t_i}, D^{\Delta t_i})$
Initialize the Kalman gain matrix, K_f
Set the sampling time, T_s for the gain update
for each iteration **do**
    Assign updated state matrix based on $R_{vc}^{\Delta t_i}$
    Obtain $K_f^{\Delta t_i}$ and assign the value
    Construct the 3D state space to provide LPV model
    if the results are satisfying **then**
        End
    else
        Retune the slope of R_{vc} and continue
    end if
end for

mathematical model of the estimator is flashed into a Simulink model likewise to the case with the constant resistor. This model is further used in the data acquisition setup for the case with updated resistance. The Simulink model for obtaining real-time estimation of i_{vc} and E_{vc}, is shown in Figure 4.11.

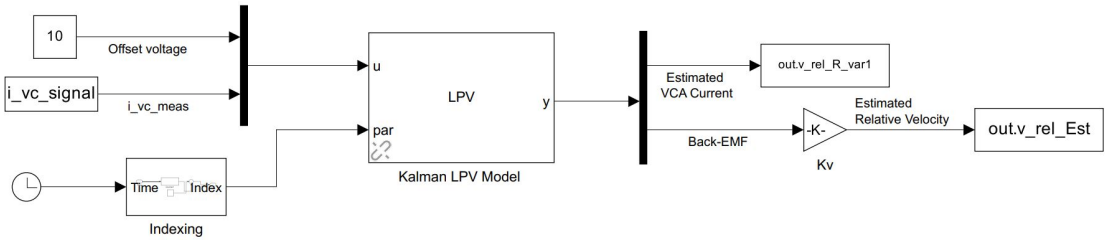

Figure 4.11: Simulink model for augmented Kalman filter wit resistance update

As can be seen, the input to the estimator is the offset voltage that is constant and the measured current across the VCA terminals. The port that is denoted with "par" is the scheduling parameter. Since the LPV model is based on the resistance update as a function of time, the scheduling parameter is basically the index that maps the time to the pertaining index. Essentially, what indexing is doing is to discretize the time coming from the clock based on the sampling time for the resistance update. The outputs of the model are the estimated quantities, namely, the estimated current, i_{vc} and the estimated back-emf, E_{vc}. A gain block is further added to the second output to convert the back-emf to the relative velocity. For the experimental validation of the approach that is employed, 5 tests are performed that the parameters R_0, T_s, and m are modified to fine tune the model. The numerical values of each parameter are reported in Table 4.2.

Test	$R_0[\Omega]$	$T_s[s]$	$m[\frac{\Omega}{s}]$
Test 1	1.485	30	0.000667
Test 2	1.46	30	0.000417
Test 3	1.46	15	0.0005
Test 4	1.47	5	0.0005
Test 5	1.485	5	0.0005

Table 4.2: Experimental tests parameters

The results from the experimental tests are summarized in Figures 4.12 to 4.16.

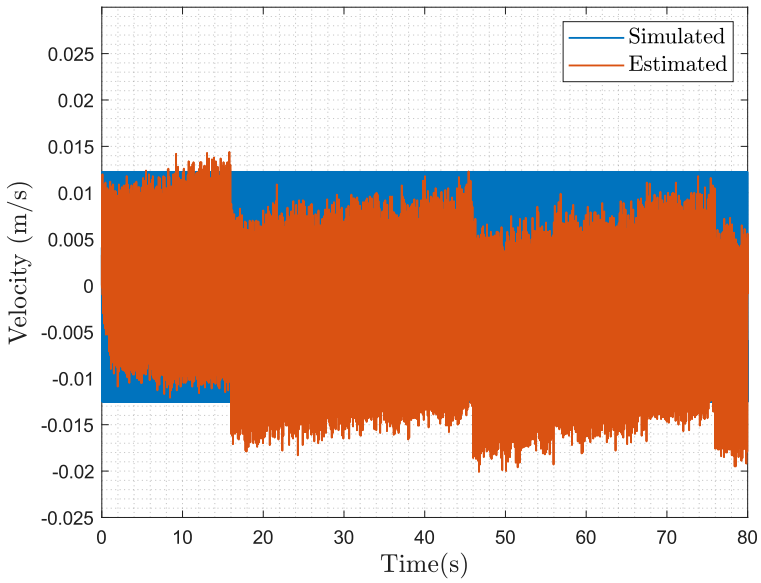

(a)

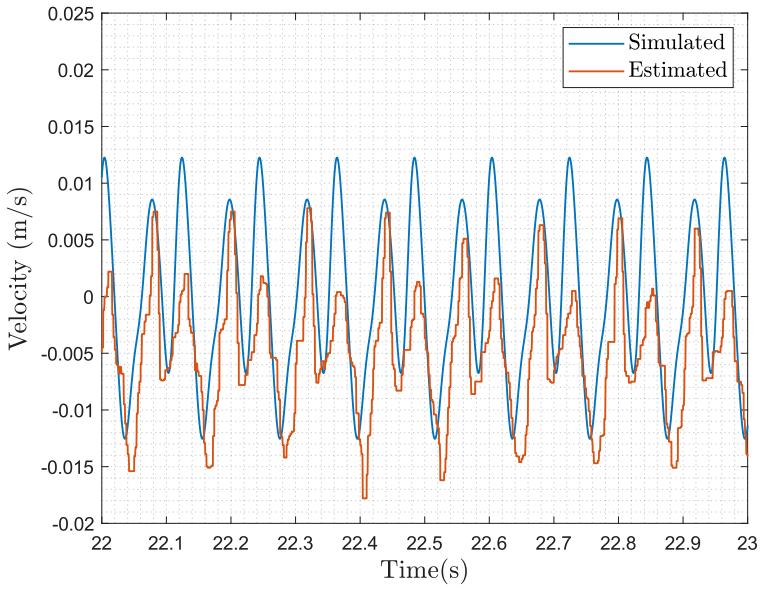

(b)

Figure 4.12: Relative velocity comparison between the simulation and AKFVG estimation from experimental data for test 1 (a) the time interval is considered to be 80 seconds to showcase the general profile of the relative velocity (drift) (b) one second snapshot of (a) for profile comparison

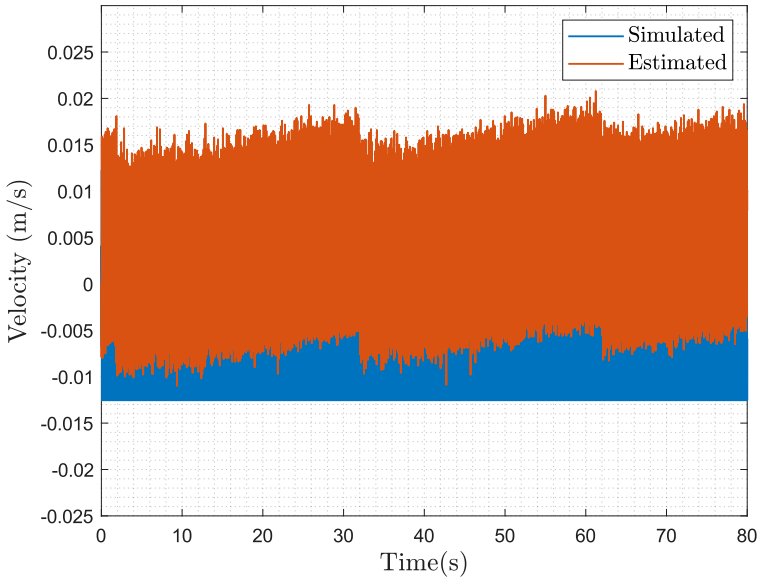

(a)

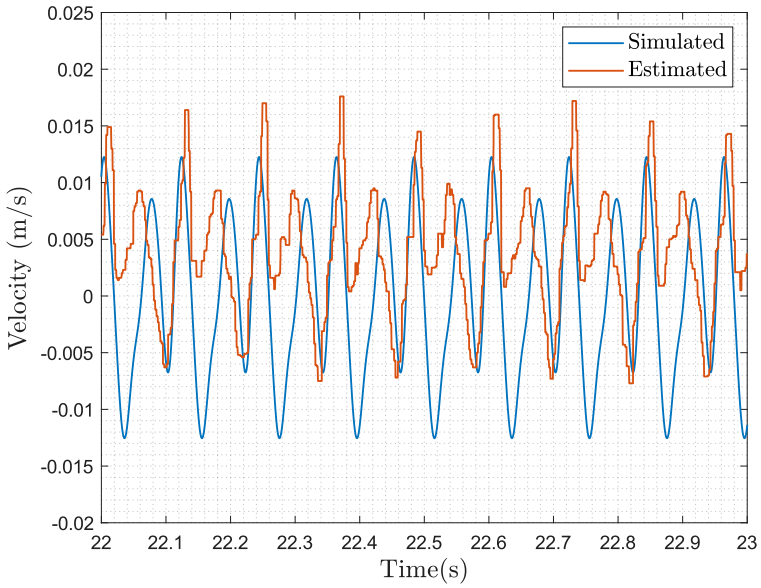

(b)

Figure 4.13: Relative velocity comparison between the simulation and AKFVG estimation from experimental data for test 2 (a) the time interval is considered to be 80 seconds to showcase the general profile of the relative velocity (drift) (b) one second snapshot of (a) for profile comparison

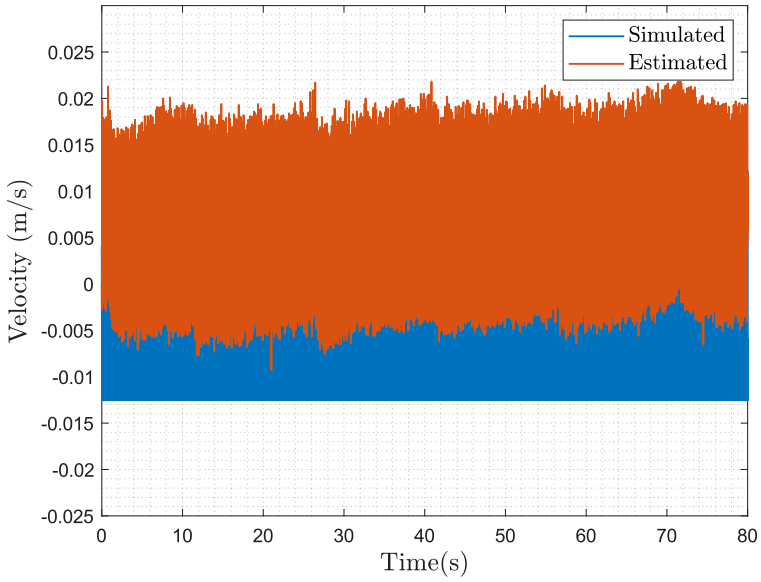

(a)

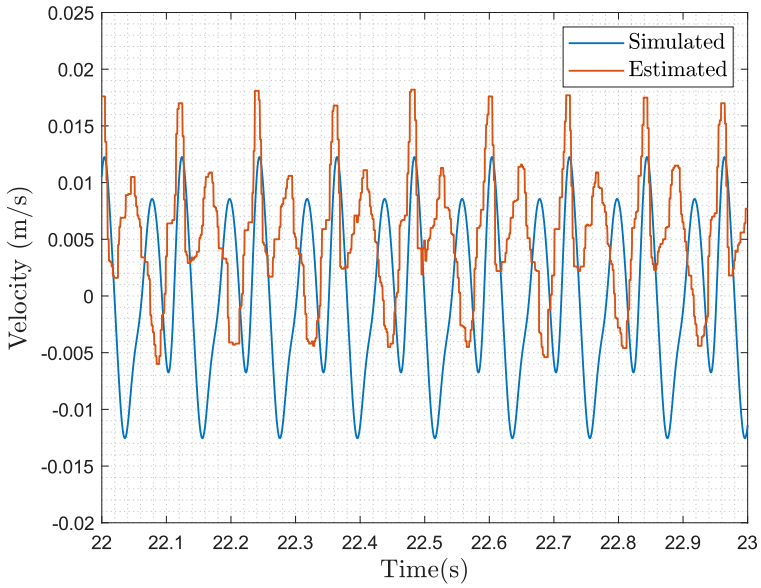

(b)

Figure 4.14: Relative velocity comparison between the simulation and AKFVG estimation from experimental data for test 3 (a) the time interval is considered to be 80 seconds to showcase the general profile of the relative velocity (drift) (b) one second snapshot of (a) for profile comparison

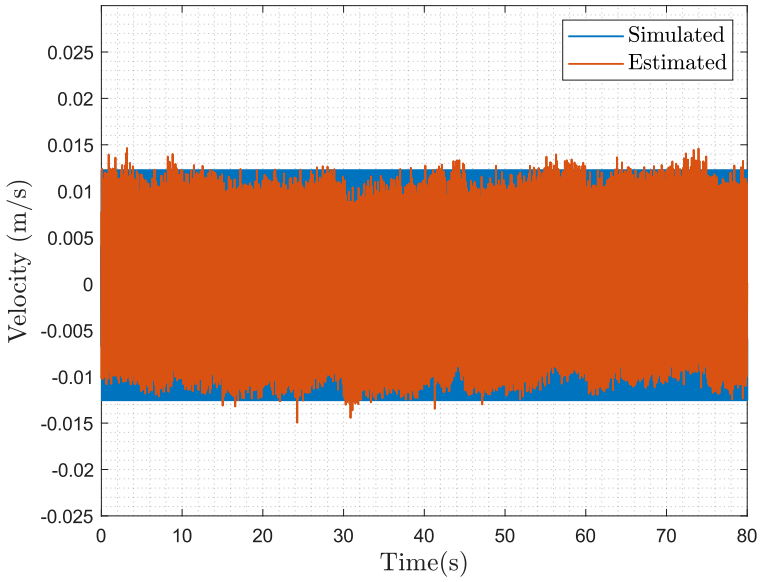

(a)

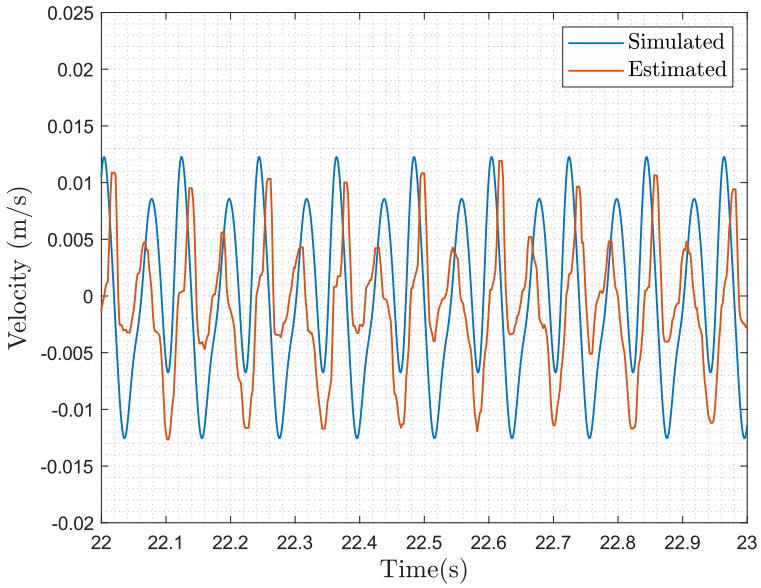

(b)

Figure 4.15: Relative velocity comparison between the simulation and AKFVG estimation from experimental data for test 4 (a) the time interval is considered to be 80 seconds to showcase the general profile of the relative velocity (drift) (b) one second snapshot of (a) for profile comparison

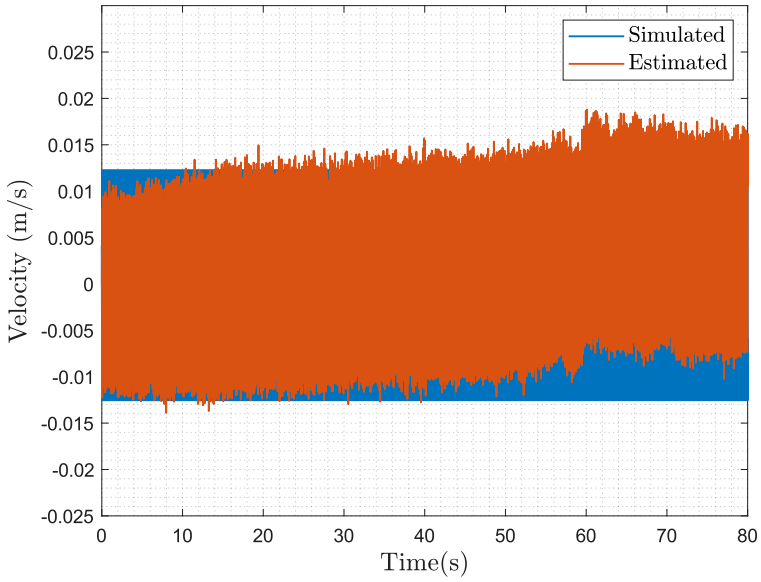

(a)

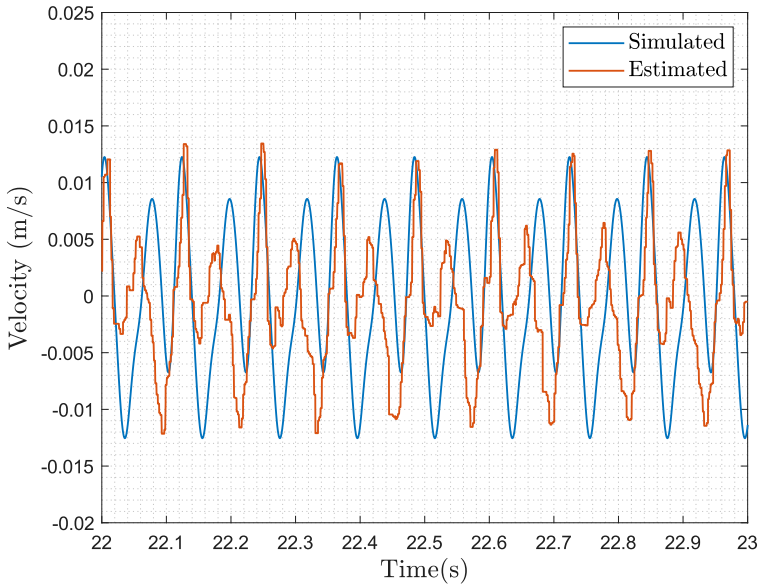

(b)

Figure 4.16: Relative velocity comparison between the simulation and AKFVG estimation from experimental data for test 5 (a) the time interval is considered to be 80 seconds to showcase the general profile of the relative velocity (drift) (b) one second snapshot of (a) for profile comparison

In test 1, the sampling time and the slope of resistance are chosen to be high. It is evident in Figure 4.12, that a sampling time of 30 seconds is not short enough to compensate the effect of resistance change that results in a saw-tooth pattern. Furthermore, higher slop of resistance change, pushes the overall trend of relative velocity downwards causing a drift downwards. For test 2 that is graphically shown in Figure 4.13, with the same sampling time but lower slope, the upward drift is not compensated that means the slope is smaller than the actual one. For test 3, as can be seen in Figure 4.14, a sampling time of 15 seconds performs better than the previous cases. Moreover the slope is considered 0.0005 $\frac{\Omega}{s}$ that is equal to the slope obtained based on the results from Figure 4.10. One can witness this is the optimal slope that keeps the general trend constant without any drift. However, poor selection of initial resistance, R_0 displays a positive offset with respect to the expected zero mean velocity. In the test 4, all the three parameters are chosen to exhibit the optimal tuning of the estimator. As illustrated in Figure 4.15, the profile of the relative velocity has a zero mean with no drift witnessed. It is worth noting that in Figure 4.15b, there is a mismatch between the simulated profile of the relative velocity and that of estimation. One pivotal reason is that for the simulation only first 5 contributing frequencies of the copper track profile considered. That means higher frequency components are disregarded for the simulation.
Observing the last test, namely the test 5 as shown in Figure 4.16, one interesting phenomenon can be noticed. After roughly 60 seconds, the trend changes. The elbow shape after 60 seconds is a proof to this claim. Considering that 5 tests being conducted consecutively, the resistance has reached its saturation point. For this reason considering a linear function for the update of the resistance is no more valid. The overall experimental results from the tests using estimator model with offline update of the resistance prove to solve the issue of the drift in the estimation of the relative velocity. This is evident in Figures 4.12 to 4.15. However, choosing the time as scheduling parameter has two drawbacks. The first one refers to the tuning of the initial resistance of the VCA, R_0, at each consecutive test, since conducting multiple tests heats up the VCA and accordingly changes the resistance of coils. The second one is addressed when the tests take long enough time that the resistance reaches its saturation point where the linear model is not valid anymore. Nevertheless, it is safe to say that for the short runs, i.e. the tests that resistance does not reach its saturation point this method performs well and well suits for control strategies that demand full-state feedback.

Chapter 5

Evaluation on MPC Performance using Estimated Relative Velocity by AKFVG

In this section, a final evaluation on MPC performance is conducted where the estimated relative velocity is being fed to the controller. Furthermore, the performance of the MPC is assessed in a scenario where there is no prior knowledge about the disturbance. Additionally, an impulse is introduced to evaluate the MPC's performance in handling transient responses.

5.1 MPC Performance Assessment in Presence of Measured Disturbance

In this scenario using the model from Appendix A.4, the performance of the MPC is evaluated by comparing the sprung mass displacement and acceleration with the case with passive damping. The main difference in this study is the feedback from the estimated relative velocity. To be more clear, for the simulation purpose the measured current from the plant along with the control input from MPC is fed into the AKFVG. Consequently, the estimated relative velocity is fedback to the MPC to close the loop. However, the remaining 4 states are assumed to be all measurable and no further estimation is needed. The results are reported in Figures 5.1 and 5.2. Comparing the z_s profile in Figures 3.8a and 5.1b, there is slight change in the magnitude and profile of the sprung mass displacement,

z_s. This is due to the fact that using an estimator alters the overall closed-loop dynamic of the system.
Furthermore, the comparison of the acceleration between the passive damping case and MPC that is presented in Figure 5.2, indicates the superiority of MPC over passive damping control from comfort point of view. The results both for acceleration and displacement of the sprung mass demonstrate that the implemented AKFVG performs well not only in the case when the input voltage is constant but also in the case that it varies according to the controller.

5.2 MPC Performance Assessment in Absence of Measured Disturbance

Unlike the track irregularities in the testbench that are measured, in most real world cases, often it is impossible to model the disturbance precisely to use in prediction model. Moreover, unanticipated disturbance such as an abrupt impulse from the track is not an unusual occurrence. For this reason the performance of the MPC is evaluated for the case that the measured disturbance is not present and the plant experiences an impulse with an amplitude of 24 N/s from the track at $t = 4.5s$. The simulation results are illustrated in Figure 5.3. It can be seen that even in the case where the disturbance is unmeasured, MPC outperforms passive damping. During the transient phase, avoids a large overshoot that is present in the passive case. This further hinders the abrupt drop after the overshoot. The settling time is considered to be equal to that passive damping case that is no more than 0.7 seconds. Eventually, in the steady state phase the amplitude of oscillations for MPC is roughly 50% of the amplitude of oscillations for the passive damping case.

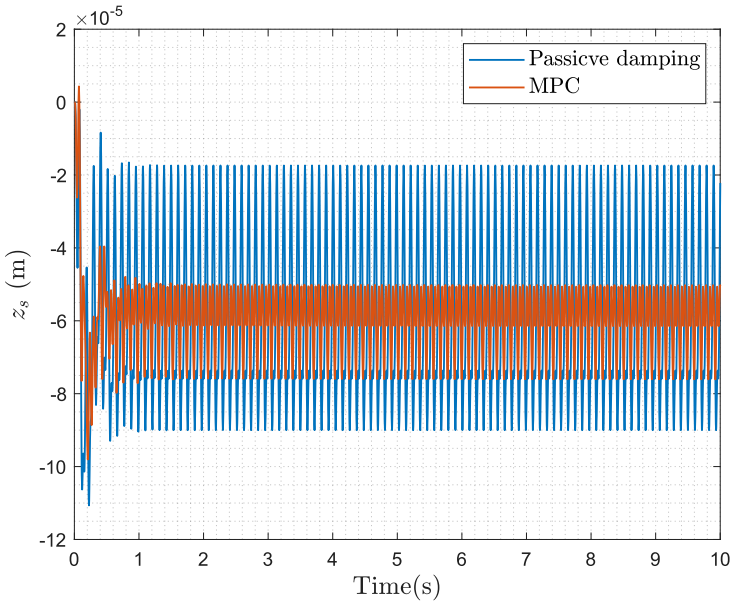

(a)

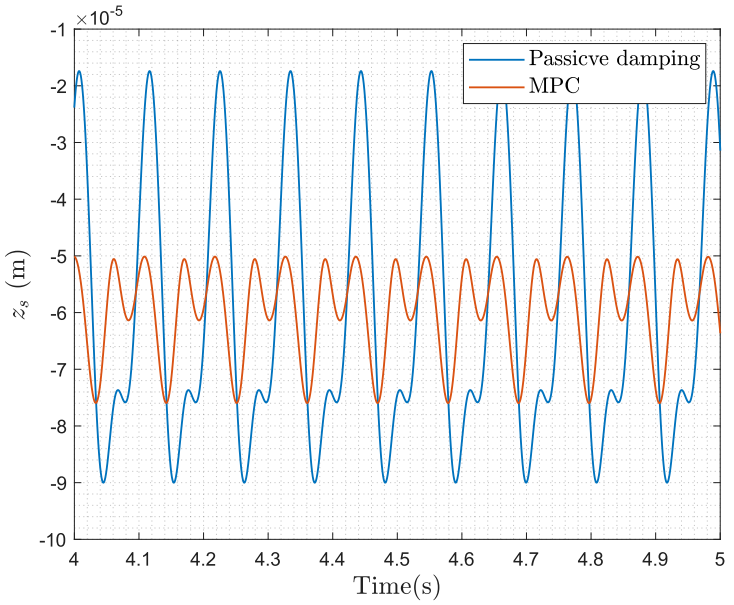

(b)

Figure 5.1: Sprung mass displacement comparison for the cases with passive damping and MPC with feedback from estimated relative velocity (a) model simulation for 10 seconds (b) zoomed view

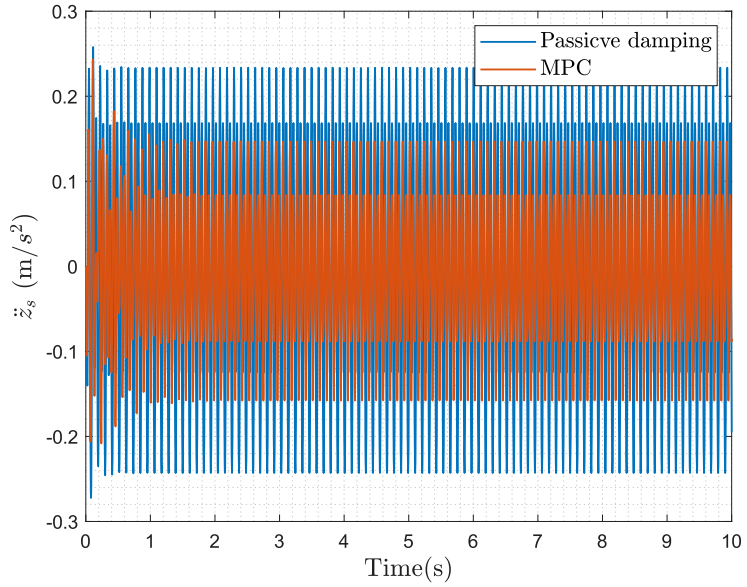

(a)

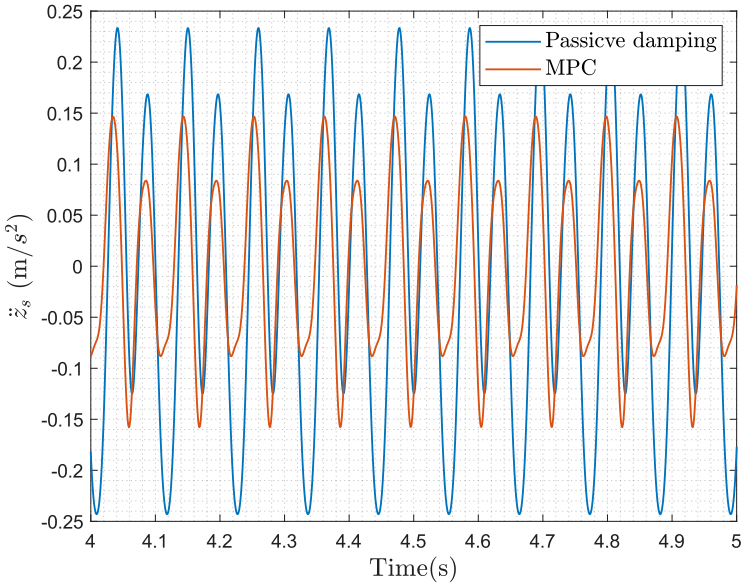

(b)

Figure 5.2: Sprung mass acceleration comparison for the cases with passive damping and MPC with feedback from estimated relative velocity (a) model simulation for 10 seconds (b) zoomed view

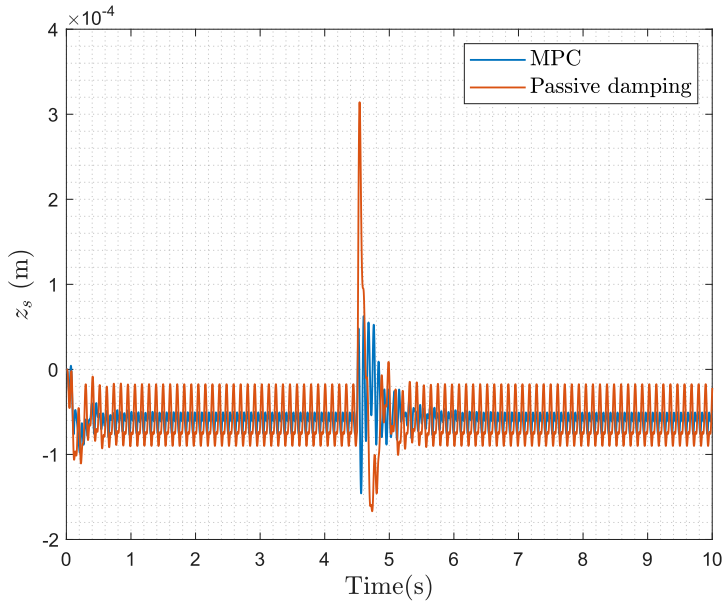

(a)

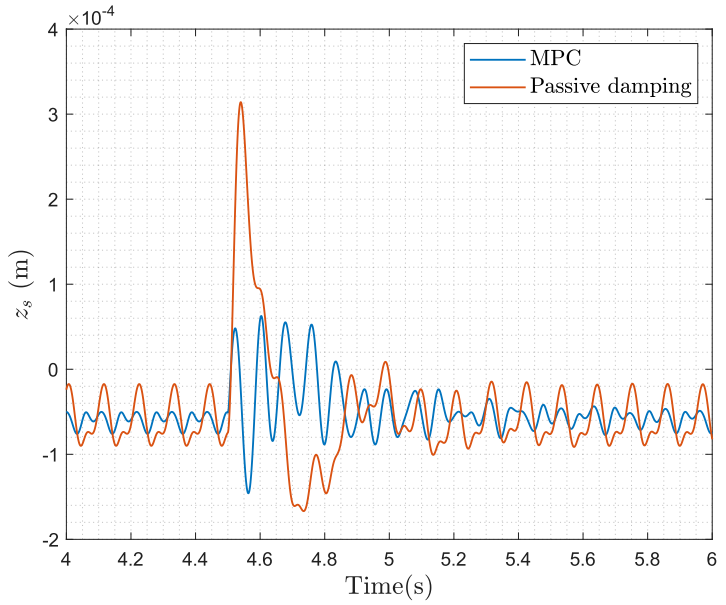

(b)

Figure 5.3: Sprung mass displacement comparison for the cases with passive damping and MPC with feedback from estimated relative velocity with no measured disturbance (a) model simulation for 10 seconds (b) zoomed view

The findings from the simulations highlight the resilience of MPC in real-world scenarios where disturbances are not explicitly modeled or known in advance. This robustness is particularly valuable in large-scale models where the track profile cannot thoroughly be measured.
In such scenarios, MPC's ability to adapt and maintain stable performance even in the absence of precise disturbance models ensures reliable control over the system's behavior. This resilience to uncertainty allows MPC to effectively handle variations and unexpected events that may arise during operation. Overall, the ability of MPC to maintain stability and performance in the face of uncertainties underscores its effectiveness as a control strategy.

Chapter 6

Final Remarks

6.1 Conclusions

The present study encompasses the design of an MPC controller to regulate the vibrations of an electrodynamic pad using a voice coil actuator. Additionally, it introduces a novel approach for estimating relative velocity based on back-emf estimation, tailored for scenarios where the physical properties of the system undergo changes.

Initially, leveraging the analogy between the model under examination and the quarter-car model utilized in automotive engineering, a 2-DOF model of the plant is developed, incorporating the electrical domain of the voice coil actuator (VCA). The primary objective is to mitigate external excitations, such as electrodynamic disturbances resulting from track irregularities, and isolate the sprung mass. In the absence of control forces, the voice coil inherently provides a damping effect due to eddy currents, acting as a passive damper. However, to enhance vibration isolation, a control strategy grounded in the predictive model of the system is implemented. MPC facilitates optimal control input by minimizing a quadratic cost function. To achieve optimal MPC performance, parameter tuning is essential, particularly weights associated with control input and states. A grid search method is employed for this purpose, revealing that assigning values of 22, 1, and 1.2 to the weights of voice coil current, voltage input, and voltage input rate, respectively, results in an 80% reduction in sprung mass displacement amplitude as well as 55% reduction in its acceleration compared to passive damping. Additionally, MPC's performance is contrasted with that of the LQR controller, with MPC demonstrating superior performance in vibration isolation.

In the second phase of the project, the challenge of measuring mechanical states, particularly relative velocity, is addressed. To tackle this issue, an augmented Kalman filter is employed, utilizing the VCA model to estimate back-emf, assuming

a constant rate of change. However, the results from experimental tests reveal a drift in the estimated relative velocity profile compared to the expected profile. This discrepancy arises due to the generation of heat and subsequent increase in resistance of the coils with the VCA, resulting from providing constant voltage to decouple the two masses. To mitigate this issue, the initial LTI model for the Kalman filter is replaced with an LPV model. This LPV model comprises a 3D matrix of individual LTI models, for which Kalman gain vectors are obtained offline and then interpolated to form the final model. Careful tuning of three parameters – the initial resistance of VCA, the slope of resistance growth, and the sampling time for resistance update – ensures the best estimation model, with final results aligning with expectations from numerical simulations.
Subsequently, a numerical simulation is conducted using real-time estimation of relative velocity and closing the loop for MPC with the estimated quantity. As anticipated, closing the control loop with the estimated quantity exhibits slightly weaker performance compared to the case with fully observed states. Nonetheless, the results demonstrate promise and validate the estimation method's suitability for use in MPC applications.

6.2 Further Work

Utilizing a linear model to update resistance over time presents practical challenges that hinder its effectiveness. Firstly, it necessitates manual tuning of the initial resistance value at the outset of each test, which can be cumbersome and time-consuming. Secondly, the linear model fails to capture resistance saturation points, as evidenced by the observed elbow shape in test 5. To overcome these limitations, a more robust and accurate resistance model is needed, one that correlates with a measurable quantity. An alternative approach involves establishing a transfer function that links the temperature of the resistor to its resistance. By integrating a temperature sensor into the test setup to provide real-time temperature data, this transfer function facilitates precise resistance updates without the need for manual tuning. This enhancement ensures greater accuracy and reliability in resistance modeling, thereby addressing the shortcomings of the linear approach.
An additional aspect to focus on pertains to the MPC. The performance of the MPC can be evaluated in the testrig to validate the numerical simulations. However, the final model of the MPC despite having a feedback from the estimated relative velocity, still depends on the absolute displacement and velocity of the sprung mass. This opens the route to study whether an estimator is capable of providing accurate estimations of all the outputs only by having the measured current and voltage. In case the estimated quantities do not meet the expectations, alternative approaches such as installing accelerometers on the masses and obtaining the mechanical states

by means of numerical integration with respect to time. In this regard, a further refinement of the MPC plant model is needed to properly update the resistance. By considering the proposed refinements on both controller and the estimator, the application of the proposed study can be further extended to the large-scale models and contributes to the passenger comfort where it is the main motivation of the the present study and the similar research fields.

Appendix A

Matrices

A.1 State Space for System with Fully Observable Mechanical States (Absolute Kinematic States)

The state space matrices used in fully mechanical system that the control input is a force applied to the masses regardless of the actuator source.

$$x_{mech} = \{\dot{z}_p, z_p, \dot{z}_s, z_s\}^T$$

$$y_{mech} = \{\dot{z}_p, z_p, \dot{z}_s, z_s\}^T$$

$$A_{\text{mech}} = \begin{bmatrix} -\frac{c_{\text{vc}}}{m_p} & -\frac{(k_s+k_p+k_{\text{us}})}{m_p} & \frac{c_{\text{vc}}}{m_p} & \frac{k_s}{m_p} \\ 1 & 0 & 0 & 0 \\ \frac{c_{\text{vc}}}{m_S} & \frac{k_s}{m_s} & -\frac{c_{\text{vc}}}{m_s} & \frac{-k_s}{m_s} \\ 0 & 0 & 1 & 0 \end{bmatrix}$$

$$B_{\text{mech}} = \begin{bmatrix} \frac{1}{m_p} & \frac{k_p}{m_p} \\ 0 & 0 \\ \frac{-1}{m_s} & 0 \\ 0 & 0 \\ 0 & 0 \end{bmatrix}$$

$$C_{\text{mech}} = \begin{bmatrix} 1 & 0 & 0 & 0 \\ 0 & 1 & 0 & 0 \\ 0 & 0 & 1 & 0 \\ 0 & 0 & 0 & 1 \end{bmatrix}$$

$$D_{\text{mech}} = \begin{bmatrix} 0 & 0 \\ 0 & 0 \end{bmatrix}$$

A.2 State Space for System with Fully Observable Electromechanical States (Absolute Kinematic States

The state space model used for the system fully observable with the absolute quantities for the kinematic states. Subscript $\{_{EM}\}$ refers to the electromachnical matrix (or vector).

$$x_{EM} = \{\dot{z}_p, z_p, \dot{z}_s, z_s, i_{vc}\}^T$$

$$y_{EM} = \{\dot{z}_p, z_p, \dot{z}_s, z_s, i_{vc}\}^T$$

$$A_{\mathrm{EM}} = \begin{bmatrix} -\frac{c_{\mathrm{vc}}}{m_p} & -\frac{(k_s+k_p+k_{\mathrm{us}})}{m_p} & \frac{c_{\mathrm{vc}}}{m_p} & \frac{k_s}{m_p} & -\frac{k_m}{m_p} \\ 1 & 0 & 0 & 0 & 0 \\ \frac{c_{\mathrm{vc}}}{m_S} & \frac{k_s}{m_s} & -\frac{c_{\mathrm{vc}}}{m_s} & \frac{-k_s}{m_s} & \frac{k_m}{m_s} \\ 0 & 0 & 1 & 0 & 0 \\ \frac{k_m}{L_{\mathrm{vc}}} & 0 & -\frac{k_m}{L_{\mathrm{vc}}} & 0 & -\frac{R_{\mathrm{vc}}}{L_{\mathrm{vc}}} \end{bmatrix}$$

$$B_{\mathrm{EM}} = \begin{bmatrix} \frac{k_p}{m_p} & 0 \\ 0 & 0 \\ 0 & 0 \\ 0 & 0 \\ 0 & \frac{1}{L_{\mathrm{vc}}} \end{bmatrix}$$

$$C_{\mathrm{EM}} = \begin{bmatrix} 1 & 0 & 0 & 0 & 0 \\ 0 & 1 & 0 & 0 & 0 \\ 0 & 0 & 1 & 0 & 0 \\ 0 & 0 & 0 & 1 & 0 \\ 0 & 0 & 0 & 0 & 1 \end{bmatrix}$$

$$D_{\mathrm{EM}} = \begin{bmatrix} 0 & 0 \\ 0 & 0 \\ 0 & 0 \\ 0 & 0 \\ 0 & 0 \end{bmatrix}$$

A.3 State Transformation Matrix

The transformation matrix used for the transformation from absolute coordinates of the unsprung mass to the relative coordinates between the two masses.

$$T = \begin{bmatrix} 1 & 0 & -1 & 0 & 0 \\ 0 & 1 & 0 & -1 & 0 \\ 0 & 0 & 1 & 0 & 0 \\ 0 & 0 & 0 & 1 & 0 \\ 0 & 0 & 0 & 0 & 1 \end{bmatrix}$$

A.4 State Space for System with Fully Observable Electromechanical Transformed States

Using the transformation matrix T, the state space model contains the relative states. Subscript $\{_{EM,T}\}$ refers to the electromachnical and transformed matrix (or vector).

$$x_{EM,T} = \{\dot{z}_r, z_r, \dot{z}_s, z_s, i_{vc}\}^T$$

$$y_{EM,T} = \{\dot{z}_r, z_r, \dot{z}_s, z_s, i_{vc}\}^T$$

$$A_{EM,T} = \begin{bmatrix} (-\frac{cvc}{mp} - \frac{cvc}{ms}) & (-\frac{ks}{ms} - \frac{kp+ks+kus}{mp}) & 0 & -\frac{kp+kus}{mp} & (-\frac{km}{mp} - \frac{km}{ms}) \\ 1 & 0 & 0 & 0 & 0 \\ \frac{cvc}{ms} & \frac{ks}{ms} & 0 & 0 & \frac{km}{ms} \\ 0 & 0 & 1 & 0 & 0 \\ \frac{km}{Lvc} & 0 & 0 & 0 & -\frac{Rvc}{Lvc} \end{bmatrix}$$

$$B_{EM,T} = \begin{bmatrix} \frac{\mathrm{kp}}{\mathrm{mp}} & 0 \\ 0 & 0 \\ 0 & 0 \\ 0 & 0 \\ 0 & \frac{1}{\mathrm{Lvc}} \end{bmatrix}$$

$$C_{EM,T} = \begin{bmatrix} 1 & 0 & 0 & 0 & 0 \\ 0 & 1 & 0 & 0 & 0 \\ 0 & 0 & 1 & 0 & 0 \\ 0 & 0 & 0 & 1 & 0 \\ 0 & 0 & 0 & 0 & 1 \end{bmatrix}$$

$$D_{EM,T} = \begin{bmatrix} 0 & 0 \\ 0 & 0 \\ 0 & 0 \\ 0 & 0 \\ 0 & 0 \end{bmatrix}$$

Bibliography

[1] Luca Marelli, Anastasios Tsakalidis, Konstantinos Gkoumas, Ahsanul Haq, Mariano Grosso, and Frantisek Pekar. *Strategic Transport Research and Innovation Agenda (STRIA) Roadmap Factsheets*. 2017. URL: https://ec.europa.eu/jrc/en/publication/strategic-transport-research-and-innovation-agenda-stria-roadmap-factsheets (cit. on p. 1).

[2] Nadine Burkhard. *Why Invent the Hyperloop?* 2014. URL: http://large.stanford.edu/courses/2014/ph240/burkhard2/ (cit. on p. 1).

[3] SpaceX. *Hyperloop Alpha*. 2013. URL: https://www.spacex.com/sites/spacex/files/hyperloop_alpha-20130812.pdf (cit. on p. 1).

[4] Richard F. Post and Dmitri Ryutov. *The Inductrack Concept: A New Approach to Magnetic Levitation*. Technical Report UCRL-ID-124115. CA: Lawrence Livermore National Laboratory, May 1996 (cit. on p. 1).

[5] J. Van Verdeghem, V. Kluyskens, and B. Dehez. «Stability and Performance Analysis of Electrodynamic Thrust Bearings». In: *Actuators* 8.1 (2019), p. 11 (cit. on p. 2).

[6] João Detoni, Fabrizio Impinna, Andrea Tonoli, and Nicola Amati. «Unified Modelling of Passive Homopolar and Heteropolar Electrodynamic Bearings». In: *Journal of Sound and Vibration* 331.19 (2012), pp. 4219–4232 (cit. on p. 2).

[7] R Galluzzi, S Circosta, N Amati, A Tonoli, A Bonfitto, TA Lembke, and M Kertész. «A Multi-domain Approach to the Stabilization of Electrodynamic Levitation Systems». In: *Journal of Vibration and Acoustics* 142.6 (Dec. 2020), p. 061004. DOI: 10.1115/1.4046952 (cit. on pp. 2, 3, 5, 7).

[8] Eugenio Tramacere, Marius Pakštys, Renato Galluzzi, Nicola Amati, Andrea Tonoli, and Torbjörn A. Lembke. «Modeling and experimental validation of electrodynamic maglev systems». In: *Journal of Sound and Vibration* 568 (2024), p. 117950. ISSN: 0022-460X. DOI: https://doi.org/10.1016/j.jsv.2023.117950. URL: https://www.sciencedirect.com/science/article/pii/S0022460X23003991 (cit. on pp. 9, 11–13, 46, 47).

[9] Lorenzo BOSICA. «Modeling and Identification of an Experimental Test Bench for the study of Electrodynamic Phenomena». Master's thesis. Politecnico di Torino, 2021/2022 (cit. on p. 15).

[10] Max Schwenzer, Muzaffer Ay, Thomas Bergs, and Dirk Abel. «Review on model predictive control: an engineering perspective». In: *The International Journal of Advanced Manufacturing Technology* 117.5 (Nov. 2021), pp. 1327–1349. ISSN: 1433-3015. DOI: 10.1007/s00170-021-07682-3. URL: https://doi.org/10.1007/s00170-021-07682-3 (cit. on p. 17).

[11] Stephen P. Boyd and Lieven Vandenberghe. *Convex Optimization*. 7th printing with corrections. Cambridge, New York, Melbourne, Madrid, Cape Town, Singapore, São Paolo, Delhi: Cambridge University Press, 2004. ISBN: 978-0-521-83378-3 (cit. on p. 17).

[12] Saša V. Raković and William S. Levine, eds. *Handbook of Model Predictive Control*. 1st ed. Control Engineering. Birkhäuser Cham, 2019, pp. XXI, 692. DOI: 10.1007/978-3-319-77489-3 (cit. on p. 18).

[13] R. E. Kalman. «A New Approach to Linear Filtering and Prediction Problems». In: *Journal of Basic Engineering* 82.1 (Mar. 1960), pp. 35–45. ISSN: 0021-9223. DOI: 10.1115/1.3662552. eprint: https://asmedigitalcollection.asme.org/fluidsengineering/article-pdf/82/1/35/5518977/35_1.pdf. URL: https://doi.org/10.1115/1.3662552 (cit. on p. 40).

[14] Yuting Bai, Bin Yan, Chenguang Zhou, Tingli Su, and Xuebo Jin. «State of art on state estimation: Kalman filter driven by machine learning». In: *Annual Reviews in Control* 56 (2023), p. 100909. ISSN: 1367-5788. DOI: https://doi.org/10.1016/j.arcontrol.2023.100909. URL: https://www.sciencedirect.com/science/article/pii/S1367578823000731 (cit. on p. 40).

[15] Ramsey Faragher. «Understanding the Basis of the Kalman Filter Via a Simple and Intuitive Derivation [Lecture Notes]». In: *IEEE Signal Processing Magazine* 29 (2012), pp. 128–132. URL: https://api.semanticscholar.org/CorpusID:206485935 (cit. on p. 42).

[16] Simon J Julier and Jeffrey K Uhlmann. «A new extension of the Kalman filter to nonlinear systems». In: *Proceedings of AeroSense: The 11th International Symposium on Aerospace/Defense Sensing, Simulation, and Controls*. Vol. 2. International Society for Optics and Photonics. 1997 (cit. on p. 44).

[17] Thomas Duriez, Steven Brunton, and Bernd Noack. «Methods of Linear Control Theory». In: vol. 116. Nov. 2017, pp. 49–68. ISBN: 978-3-319-40623-7. DOI: 10.1007/978-3-319-40624-4_3 (cit. on p. 44).

[18] Bastian Chappuis, Serge Gavin, Luca Rigazzi, and Mauro Carpita. «Speed Control of a Multiphase Active Way Linear Motor Based on Back EMF Estimation». In: *IEEE Transactions on Industrial Electronics* 62.12 (2015), pp. 7299–7308. DOI: 10.1109/TIE.2015.2463762 (cit. on p. 46).